



Multi-temporal high-resolution imaging spectroscopy with hyperspectral 2D imagers – From theory to application

Helge Aasen^{a,*}, Andreas Bolten^b

^a Crop Science Group, Institute of Agricultural Sciences, ETH Zurich, 8092 Zurich, Switzerland

^b GIS and RS Research Group, Institute of Geography, Department of Geoscience, University of Cologne, 50923 Cologne, Germany

ARTICLE INFO

Keywords:

Specific field of view
Unmanned aerial vehicle (UAV)
Bidirectional reflectance distribution function (BRDF)
Field spectroscopy
Low-altitude remote sensing
Mosaicking
Field phenotyping
Precision agriculture
Vegetation indices
Chlorophyll

ABSTRACT

With the increasing availability of spectral sensors and consumer-grade data processing software, a democratization of imaging spectroscopy is taking place. In particular, novel lightweight 2D spectral imagers in combination with UAVs are increasingly being adapted for imaging spectroscopy. In contrast to traditional line-scanners, these sensors capture spectral information as a 2D image within every exposure. With computer vision algorithms embedded in consumer grade software packages, these data can be processed to hyperspectral digital surface models that hold spectral and 3D spatial information in very high resolution. To understand the spectral signal, however, one must comprehend the complexity of the capturing and data processing process in imaging spectroscopy with 2D imagers.

This study establishes the theoretical background to comprehend the properties of spectral data acquired with 2D imagers and investigates how different data processing schemes influence the data. To improve the interpretability of a spectral signal derived for an area of interest (AOI), the specific field of view is introduced as a concept to understand the composition of pixels and their angular properties used to characterize a specific AOI within a remote sensing scene.

These considerations are applied to a multi-temporal field study carried out under different illumination conditions in a barley field phenotyping experiment. It is shown that data processing significantly affects the angular properties of the spectral data and influences the apparent spectral signature. The largest differences are found in the red domain, where the signal differs by approximately 10% relative to a single nadir image. Even larger differences of approximately 14% are found in comparison with ground-based non-imaging field spectrometer measurements. The differences are explained by investigating the interaction between the angular properties of the data and canopy anisotropy, which are wavelength and growth stage dependent. Additionally, it is shown that common vegetation indices cannot normalize the differences and that the retrieval of chlorophyll is affected. In conclusion, this study helps to understand the process of imaging spectroscopy with 2D imagers and provides recommendations for future missions.

1. Introduction

Since the definition of imaging spectroscopy by Goetz (2009) and Goetz et al. (1985) as “the acquisition of images in hundreds of contiguous, registered, spectral band,” the field has greatly developed. In recent years, unmanned aerial vehicles (UAVs) have become an increasingly used platform for photogrammetry and remote sensing (Colomina and Molina, 2014; Pajares, 2015). Particularly when combined with specialized sensors, they become powerful sensing systems for gathering up-to-date information about vegetation. Their low flying altitude allows them to capture data at very high spatial resolution. The advent of small and lightweight spectral sensors has also boosted this

development for imaging spectroscopy. Spectral line scanners have been used to detect biotic (Calderón et al., 2013) and abiotic stress, chlorophyll content (Lucieer et al., 2014b; Malenovsky et al., 2015; Zarco-Tejada et al., 2012) and nitrogen uptake (Quemada et al., 2014).

Lately, 2D spectral imagers are also being increasingly used. These sensors capture radiometric and spectrally characterized information as a 2D image within every exposure (Aasen et al., 2015). In particular, with the advent of consumer-grade software tools that incorporate recent photogrammetric algorithms for structure from motion (SfM), imaging spectroscopy with 2D imagers has become possible for a wide audience. With SfM, the relative position and orientation of 2D images can be estimated as long as the scene shows sufficient texture and the

* Corresponding author.

E-mail addresses: helge.aasen@usys.ethz.ch (H. Aasen), andreas.bolten@uni-koeln.de (A. Bolten).

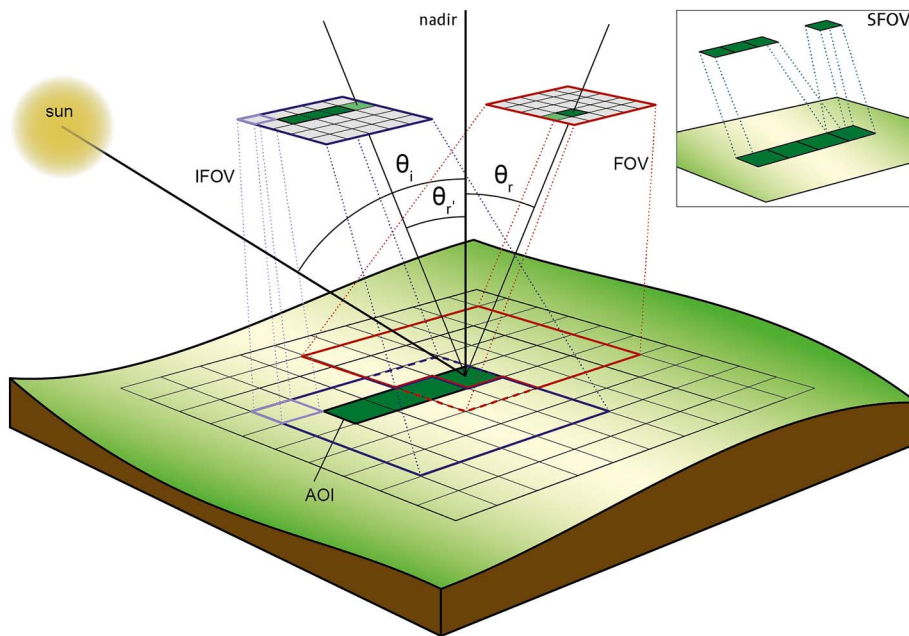


Fig. 1. Schematic drawing of imaging spectroscopy with 2D imagers with the field of views (FOVs) of two images (simplification of the normal case with multiple overlapping images) and an instantaneous field of view (IFOV) of one pixel. Each pixel within an image is recorded with different angular properties. The same surface area may be captured by several pixels with different angular properties (as denoted by the zenith reflectance angles θ_i and θ_r for one pixel. For clarity, the azimuth angles are omitted). Additionally, the concept of the specific field of view (SFOV) of an area of interest (AOI) on the ground within a hyperspectral digital surface model is shown. The SFOV describes the pixels and their angular properties that are used to characterize an AOI (excerpt top right).

images are recorded with a sufficient overlap. This allows the joining of these images to create a full scene. Additionally, the 3D geometry can be reconstructed to derive digital surface models (DSMs) (Remondino and El-Hakim, 2006; Szeliski, 2011). Thus, SfM has become the standard procedure to process 2D RGB (e.g., Bendig et al., 2015; Dandois and Ellis, 2010; Geipel et al., 2014; Lucieer et al., 2014a; Roth and Streit, 2017; Whitehead and Hugenholtz, 2015), as well as spectral scenes (e.g., Aasen et al., 2015; Honkavaara et al., 2013, 2009; Jakob et al., 2017; Näsi et al., 2015).

Still, the properties of spectral data acquired with 2D spectral imagers have received little attention. While Aasen et al. (2015) investigated the influence of the camera system, the interaction of different measurement geometries of pixels, canopy anisotropy and illumination conditions with the data processing procedures to retrieve full scenes from the individual images have hardly been investigated. Further, non-imaging spectrometers are still widely used at ground level to develop models for remote sensing applications (Milton et al., 2009), such as biomass (Aasen et al., 2014; Gnyp et al., 2013; Hansen and Schjoerring, 2003; Marshall and Thenkabail, 2015), LAI (Haboudane et al., 2004) and pigments (Gitelson and Merzlyak, 1994; Haboudane et al., 2002; Yu et al., 2014). But only very few studies (Bareth et al., 2015; Domingues Franceschini et al., 2017; Hueni et al., 2016; von Bueren et al., 2015) have included a dedicated comparison of imaging with non-imaging data for vegetated areas. If data from different sensors should be used in an integrative approach and UAVs should unfold their foreseen potential to bridge the gap between ground, airplane and satellite observations, the differences between data derived from different sensors and processed in different ways must be understood. Additionally, UAVs are seen as tools for frequent multi-temporal observations to gather the necessary near real-time information for precision agriculture and field-phenotyping applications (Araus and Cairns, 2014; Berni et al., 2009; Fiorani and Schurr, 2013); however, this also demands flights under different illumination conditions. Finally, yet importantly, while the increasing availability of spectral sensors and consumer-grade software packages carries the potential a democratization of imaging spectroscopy—allowing research groups, companies and even individuals to gather their own data—spectral data acquisition and processing is not trivial. Thus, these processes must be fully comprehended.

Motivated by this situation, this study investigates the workflow of imaging spectroscopy with 2D imagers. First, a theoretical background

to understand the properties of the data and the influence of the processing scheme on the data in the full scene is established. Second, the common theory for imaging spectroscopy is advanced by the specific field of view (SFOV) to comprehend how the spectral signature of an area of interest (AOI) on the ground is composed, and how it is influenced by scene generation. Third, the complex interaction of the data properties, data processing, vegetation structure and illumination conditions are investigated based on a multi-temporal study of a spring barley experiment. Additionally, the data are compared to ground-based non-imaging observations.

2. Imaging spectroscopy with 2D imagers

2.1. Data properties

Imaging spectroscopy with 2D imagers generates a spectral representation of a scene by recording multiple overlapping images, which are then composed into the full scene based on a particular processing scheme (e.g., Aasen et al., 2015; Honkavaara et al., 2013). The exact composition depends on the flight trajectory and capturing position of each image, as well as the processing scheme used to generate the final scene. Each image contains a representation of the spectral properties of the objects within the sensor's field of view (FOV) at the particular capturing position and orientation during the measurement. Additionally, each image consists of individual pixels that have their own instantaneous field of view (IFOV), and consequently, each pixel has its own measurement geometry. Fig. 1 illustrates this for two overlapping images.

In remote sensing, the reflectance of a surface is commonly expressed as the ratio of the flux received within the conical (I) FOV of a sensor from the sampled surface and a lossless and Lambertian reference surface in the same beam geometry under natural illumination conditions. Thus, these measurements are precisely referred to as hemispherical conical reflectance factors (HCRF; Schaepman-Strub et al., 2006). This is particularly true for field spectrometers with a rather wide FOV. The pixels of imaging spectrometers have fairly small IFOV, which also results in a rather small measurement cone for each pixel. Therefore, their measurements can be considered as an approximation of directional measurements (Schläpfer et al., 2015) and the resulting quantities as hemispherical directional reflectance factors (HDRF). Eq. 1 gives the formula for the reflectance factor of a pixel (x

and y denote the geographic position of this pixel) with θ as the zenith and ϕ as the azimuth angle of the incident (i) radiation over the hemisphere (2π) and reflected (r) radiation and the solid angle of the IFOV (ω_r), which for the HDRF case is set (close) to 0. For simplicity, the reflectance factors measured in this study are mostly referred to as reflectance.

$$R_{x,y}(\theta_i, \phi_i, 2\pi, \theta_r, \phi_r, \omega_r) \quad (1)$$

2.2. Data processing

Every pixel at a certain geolocation (or voxel in the case of a 3D representation) in the final scene is covered by multiple images. During the generation of a scene, the processing scheme defines the function of how the images are composed to the final scene; consequently, how the spectral information of the pixels in the final scene is generated from the pixels of the individual images (Eq. 2).

$$R_{x,y}^{scene} = f(R_{x,y}^{images}) \quad (2)$$

The information assigned to a pixel in the final scene is taken from one image or multiple images. When only one image per pixel is taken into account, each pixel within the scene has its own angular properties defined by the measurement geometry of the individual pixel during the acquisition of the corresponding image. When multiple images are taken into account, pixel values with different angular properties are composed. Thus, the angular properties of a pixel in the resulting data product are a composition of the angular properties of the pixels of from the individual images.

2.3. Specific field of view

Within an individual image, the measurement geometry can be calculated as long as the IFOV, the image orientation and position, and the surface geometry are known. To generate a scene, the images are composed depending on the orientation and position of the individual images defined by the flight trajectory and the capturing position. An AOI within a scene might be covered by several pixels that are eventually captured in different images. Thus, the spectrum to characterize this AOI is also composed of multiple pixels and their composition of angular properties. In the following, the composition of pixels and their angular properties within a scene used to characterize a specific AOI on the ground is called the specific FOV (SFOV). Fig. 1 illustrates this concept. The area within the scene is covered by two images (simplification of the normal case with multiple overlapping images). Within these images, each pixel has its own angular properties resulting from the measurement geometry. Moreover, the same area might be covered by pixels from different images with different angular properties. Depending on the composition of the spectral information within the scene, an AOI is characterized by the SFOV composed of pixels from several images. Formally, the SFOV of an AOI can be expressed as the mean of the reflectance quantities of a number of pixels n within the AOI (Eq. 3). This function defines how the spectral information about the AOI is calculated from the individual reflectance factors.

$$\text{specific field of view of an area of interest: } SFOV_{AOI} = \frac{1}{n} \sum_n R_{x,y,n}; R_{x,y} \in \text{AOI} \quad (3)$$

This becomes important when anisotropic surfaces such as plant canopies are measured. Depending on vegetation properties such as leaf angle, leaf area and canopy structure and their interaction with the incident irradiance and illumination regime, light is heterogeneously reflected to the hemisphere. Thus, the apparent reflectance perceived by a sensing system is dependent on the measurement geometry (Qi et al., 1995; Schaepman-Strub et al., 2006; Zhao et al., 2015). This effect is usually described with the bidirectional reflectance distribution

function (BRDF; Nicodemus et al., 1977; Schaepman-Strub et al., 2006). As described above, this becomes complex for imaging spectroscopy data, since the geometric sun-surface-sensor properties are unique for every pixel and depend on the IFOV of that specific pixel. In particular, for imaging spectroscopy with 2D imagers, the geometrical factors must be considered in two spatial dimensions. To understand the information within a remote sensing scene generated by imaging spectroscopy that is eventually measured with different measurement geometries, these interactions must be understood.

3. Case study

Imaging spectroscopy with 2D imagers is complex and multiple effects may influence the data. To comprehend these effects, a multi-temporal field study under different illumination conditions is described. In the following sections, this case study and the materials and methods to demonstrate the theoretical considerations are introduced.

3.1. Field experiment and ground data collection

The field campaigns were carried out on a barley experiment at the University of Bonn's research station, Campus Klein-Altendorf (50°37,51' N; 6°59,32' E), within the CROP.SENSE.net project (www.cropsense.uni-bonn.de/) in 2014. In total, nine varieties of barley were cultivated with two nitrogen treatments (40 kg/ha, 80 kg/ha) three times. In this study, six different varieties in 32 plots were considered. The size of each experimental plot was 3 × 7 m. Each plot was divided into two parts: in one part, the destructive measurements were carried out. Leaf chlorophyll concentration was estimated by collecting three stamps with a radius of 3 mm from four leaves at the top layer of the canopy within the destructive sampling part of each plot. These were instantly frozen with liquid nitrogen and chlorophyll was estimated by the DMSO method (Blanke, 1992) at the Institute of Crop Science and Resource Conservation (INRES), University of Bonn. In the remaining part of the plot, non-destructive remote sensing measurements were taken. To exclude border effects and tractor tracks, a 0.8 m distance to the plot border was utilized.

Additionally, field spectrometer measurements were carried out with a FieldSpec3 (FS3; ASD Inc., www.asdi.com). It covers a spectral range of 350 to 2500 nm with an FWHM of 3 nm (VNIR) to 10 nm (SWIR). The spectra are resampled to 1 nm resolution by the software of the manufacturer. Each measurement spatially integrates one spectrum for the entire FOV. The FS3 was used without a fore optic, resulting in an FOV of 25°. Measurements with the FS3 were taken with a common measurement procedure including regular optimization and calibration with a white Spectralon panel to adapt to illumination changes. For details, please refer to Tilly et al. (2015). Within each plot, 10 measurements were taken at six random positions.

3.2. Hyperspectral digital surface generation

3.2.1. UAV sensing system

The UHD 185-Firefly (UHD; Cubert GmbH, www.cubert-gmbh.de) is a hyperspectral snapshot camera. Snapshot cameras are 2D spectral imagers but distinguish themselves from other spectral sensors by recording a two-dimensional hyperspectral image within a single exposure and thus do not use any scanning process. The UHD records 138 spectral bands from 450 to 950 nm with a spatial resolution of 50 × 50 pixels. In total, 2500 spectra per band are recorded simultaneously. The FWHM ranges from approximately 5 to 25 nm. Additionally, a grayscale image with 1000 × 990 pixels is recorded simultaneously with the hyperspectral image using the same camera through the same lens. The FOV of the camera is 20° across- and along-track. At 30 m above ground flying altitude, this results in a spatial ground resolution of hyperspectral information of approximately 20 cm and 1 cm for the grayscale image. The IFOV for every pixel is approximately 0.4°. The camera is

mounted on a gimbal (MK HiSight SLR2, www.mikrokoetter.de), which compensates for pitch and roll movement and therefore ensures a nadir orientation of the camera. A single board computer controls the camera and records the data. The camera and single board computer are carried on a multirotor UAV (MK OktoXL 2, www.mikrokoetter.de). For details on the image capturing system and the UAV, please refer to Aasen et al. (2015).

3.2.2. Hyperspectral snapshot camera data processing

Before each flight, a reference image is taken by placing the camera and UAV above a white calibration panel (95% reflectance Zenith Lite). After dark current correction, this image is used to convert the raw digital numbers of each image taken during the flight to reflectance. Then, a special image cube is generated as introduced by Aasen et al. (2015). Because the grayscale and spectral image capture the same area on the ground, they can be merged by increasing the resolution of the spectral image with the nearest neighbor algorithm to match the gray image's resolution. The data is then stacked in a multi-tiff. Merging the high-resolution grayscale and low-resolution spectral image is necessary as the spatial resolution of the spectral data is too low to apply the SfM procedure. The individual image cubes are loaded into Photoscan (Professional Edition, version 1.1.6, www.agisoft.com) and processed with the typical workflow: after initial photo alignment, the scene is georeferenced by GCPs measured with a differential GPS (TOPCON Hiper Pro, www.topcon.eu) with a precision of approximately 1 cm. Then, a dense point cloud (ultra-high) is created. At this stage, an HS dense point cloud is created. Thus, in contrast with traditional approaches, the HS and 3D information is linked inherently throughout the processing and no further post-processing is needed. The hyperspectral and 3D spatial data are exported with a spatial resolution of 5 cm. The combination of the 3D and spectral data is called a hyperspectral digital surface model (HS DSM) and is a representation of the 3D surface linked with hyperspectral information emitted and reflected by the objects covered by the surface (Aasen et al., 2015). In total, 294, 198, 353 and 335 images are processed for the campaigns at 56, 70, 84 and 96 days after seeding (DAS), respectively. The measurement parameters and conditions are summarized in Table 1.

Photoscan allows exporting the spectral data with different processing modes. To investigate the influence of the processing modes, the spectral data are exported twice. The first export is performed with the blending mode 'disabled' (HS DSM_{dis}). In this mode, the spectral information is taken from the image whose center is closest to the pixel in the composed scene. Thus, the spectra are not modified and each pixel has the original spectral information. The second export is performed in blending mode 'average' (HS DSM_{avg}). Here, the information from all available images is taken and averaged for the calculation of the pixels' spectral information in the composed scene. The different processing modes only influence the spectral data. Thus, below, the terms HS DSM_{dis} and HS DSM_{avg} refer to the spectral data of the HS DSMs.

3.3. Influence of the data processing scheme

To investigate the influence of the data processing scheme, the spectral information of the area of plot 35 at DAS 70 is extracted from the HS DSM_{dis}, HS DSM_{avg} and a single image that covers the plot in a

close to nadir viewing geometry. To comprehend the composition of images within the HS DSM_{dis}, the position of pixels within the original image is used. The technique was developed in Aasen et al. (2015) and allows tracing the position of a pixel in the individual image into the composed scene. This pixel position is given in pixels along the along- and across-track direction of the UAV since the camera was mounted parallel to the flight direction. Low pixel positions in the across-track direction are on the north side of the image and their measurement geometry is more acute to the sun (cf. Fig. 3). In the across-track direction, low pixel positions are on the east side. The pixel position allows the comprehension of the viewing geometry of an individual pixel. Additionally, because the time of the flight is known (cf. Table 1) and the scene is orthorectified, the sun's position relative to the scene can be comprehended. Additionally, the pixel-position allows the identification of the edges of the individual images in the HS DSM_{dis}. Further, the HS DSMs provide information about the canopy height. Combining the information on the measurement geometry, canopy height and illumination helps to comprehend the differences in the data products generated by the different processing modes.

3.4. Influence on the specific field of view

The data processing technique also influences the SFOV that is used to characterize an AOI. With the pixel tracing technique, the composition of the SFOV can be reconstructed. The pixel position is extracted and visualized as a two-dimensional histogram showing the distribution of pixel position within the SFOV of plot 35 at DAS 70 for the HS DSM_{dis} in relation to the total FOV of the UHD. Similarly, the positions of all pixels covering the same plot are extracted from all images used for the HS DSM_{avg}.

To investigate the influence of different SFOVs on the spectral information, the spectra for plot 35 at DAS are extracted from the HS DSM_{dis} and HS DSM_{avg}. These spectra are compared to spectral information extracted from the single nadir image of the same area and spectral information collected with the FS3 on the ground. To show the relative difference between the spectra, they are normalized (divided) by the spectral information of the single image. The resulting quantities are similar to anisotropy factors (ANIF; Sandmeier et al., 1999) but for the entire AOI, since they express the relative difference of the spectral information in comparison to the information extracted from the nadir image. To explain the results, the impact on the spectral information of the canopy cover, measurement geometry and illumination are investigated.

3.4.1. Impact of canopy cover

At DAS 56, cloudy conditions suppressed effects from direct illumination. To investigate the impact of the canopy cover on the difference between the two processing modes, the spectral information of a densely and sparsely vegetated plot are extracted from the HS DSM_{dis} and HS DSM_{avg} and divided by each other. To comprehend the differences, the measurement geometries of the SFOV in the HS DSM_{dis} and HS DSM_{avg} are investigated.

3.4.2. Impact of measurement geometry and illumination

To investigate the impact of the different measurement geometries

Table 1

Summary of the dates with corresponding days after seeding (DAS), parameters and environmental conditions during the UHD campaigns. Additionally, the date of the field spectrometer (FS3) measurements and plant parameter (PP) extraction are shown.

UHD	FS3	PP	DAS	Growth stage	UHD weather	Take off time	Image count	Sun elevation	Sun azimuth
6-May	6-May	8-May	56	Stem elongation	Cloudy	10:30	294	40.62°	117.1°
20-May	22-May	22-May	70	Booting	Sunny	13:30	198	59.35°	180.42°
3-Jun	2-Jun	5-Jun	84	Heading	Sunny	12:50	353	60.56°	160.57°
12-Jun	18-Jun	17-Jun	96	Development of fruit	Sunny	12:30	335	59.97°	150.41°

of the HS DSM_{dis} and HS DSM_{avg} measurement geometry on the spectral information, the difference in the average measurement geometry per plot is correlated with the relative difference in spectral information retrieved from the two data products for all DAS and wavelength. For this, the difference between the average position of all pixels within the SFOV for all plots in the HS DSM_{dis} and HS DSM_{avg} is calculated. A negative difference shows that the information in the HS DSM_{dis} has been recorded from a more acute angle to the incoming beams of the sun and vice versa. Additionally, the ratio of the reflectance between the spectral information of the HS DSM_{dis} and HS DSM_{avg} is calculated for all plots. A ratio larger than 1 shows that the apparent reflectance in the HS DSM_{dis} is greater than in the HS DSM_{avg}. For each wavelength, this ratio is correlated with the difference in average pixel position for all wavelength and DAS.

3.5. Radiometric calibration

Due to the mechanical instability of the camera prototype and several maintenance issues during the year 2014, the camera could not be radiometrically calibrated in a general manner. Additionally, the camera has no irradiance sensor. Thus, a calibration procedure similar to field spectrometer measurements but also common for UAV spectral sampling (Aasen et al., 2015; Bareth et al., 2015; Suomalainen et al., 2014) was applied. Before each flight, the UHD was pointed towards a reference panel to measure the down-welling solar irradiance on the panel. Then, this measurement was used to transform the DN values to reflectance; however, this type of calibration is prone to errors. At DAS 56, a significant offset in reflectance is noticed compared to the other dates (cf. Fig. 10) that cannot be explained by plant growth. Because the sky was clouded on this date, the influence of the illumination conditions during the calibration is investigated.

The fiber of the FS3 is mounted on a tripod 50 cm above a Zenith Lite calibration panel and the reflected radiation is measured. The UAV is then placed right above the downwards-facing fiber in a similar position to that used during the in-field calibration and another measurement is taken. The difference represents the influence of the UAV on the radiation reflected from the panel. Accordingly, a sensing system mounted below the UAV will also perceive the influenced radiation instead of the real radiation. Consequently, a reference image taken under these conditions would influence all measurements. To estimate the influence of the illumination conditions, the measurements are carried out under clear sky and cloudy conditions. In both cases, no direct shadow is cast on the reference panel. Under the clear sky conditions, additional measurements are taken with the person holding the UAV standing in and perpendicular to the principal plane of the sun.

3.6. Comparison to proximal non-imaging and destructive measurements

To compare the imaging to the non-imaging data, all pixels within the non-destructive part of the plot (c.f. Fig. 2) are average and a linear regression model is established with the non-imaging FS3 data for each wavelength and date. Additionally, the common VIs NDVI (Rouse et al., 1974), TCARI/OSAVI (Haboudane et al., 2002), PRI (Gamon et al., 1992) and REIP (Guyot et al., 1988), often used for chlorophyll estimation, are calculated for the HS DSM and FS3 data and compared. The formula with the spectral bands adapted to the UHD are found in Table 2.

Additionally, models of the VIs and the destructively measured chlorophyll values for single and the multiple-dates DAS 70–96 and 84–96 are established. Only plots that are entirely covered by the HS DSM are considered in the analysis. The analysis is carried out with R (R Core Team, 2016).

4. Results and discussion

4.1. Influence of the data processing scheme

The data processing scheme defines how the spectral data are composed within the HS DSM. Fig. 3 visualizes the data resulting from different processing modes. Fig. 3(A) shows the spectral information taken from only a single image at 670 nm. Fig. 3(B) shows the spectral information from the HS DSM_{avg} and Fig. 3(C) the HS DSM_{dis}. Fig. 3(D) demonstrates the composition of the HS DSM_{dis} by showing the along-track position of the pixels within the original images and thus highlights the edges of these images. Fig. 3(E) shows the average plant height within 5 by 5 cm squares. Additionally, the drawing in the bottom left schematically demonstrates the measurement geometries within an image with respect to the pixel's position. In the following section, the difference in the data generated by the different processing modes will be discussed based on the theoretical framework introduced in Section 2. Section 4.2 will then quantify the impact on the hyper-spectral data.

In the south-west part of the plot (red edging, Fig. 3D), the same reflection pattern can be seen in the single image and the HS DSM_{dis} (Fig. 3A and C). Here, the spectral information of the single image is used in the HS DSM_{dis} (image 2, c.f. Fig. 3D). In other regions of the plot, edges are visible in the spectral data of HS DSM_{dis} that do not align with the single image. These occur at the transition between the images. In particular, they are visible at the edges of images 1 and 3 (Fig. 3C and D). During the flight at DAS 70, the sun had an elevation of approximately 59° and an azimuth angle of 180°. Thus, the along-track direction of the images was approximately aligned with the solar principal plane. Here, pixels with a lower pixel position value in the y-direction were captured with a more acute angle to the incoming radiation of the sun, closer to the reflection hotspot, resulting in higher reflectance than pixels with a higher pixel position value. In the HS DSM_{avg}, these edges are not visible (Fig. 3B) due to the averaging performed during the processing for this data product. Still, a pattern is visible within the plot. The pattern is similar both to the data of the single image and the HS DSM_{dis} but is less pronounced. Overall, the reflectance to the south of the plot is higher than to the north, which can be explained by the shading of the higher canopy elements in the middle of the plot.

Although the pattern in the single image and the HS DSM_{avg} look most reasonable when compared to the pattern of the canopy height, all processing schemes have their advantages and drawbacks. The single image is chosen such that the viewing geometry is almost nadir and the plot covers only a small portion of the entire image. Aasen (2016b) showed that within a single image of a 2D imager, BRDF effects may have a strong influence. Consequently, although not directly visible in the image, the information may still be influenced by the different measurement geometries of the pixels. In particular, this effect increases when the AOI covers a larger part of the image. Additionally, nadir looking images may not be available for all regions of interest within a scene. While the averaging in the HS DSM_{avg} may equalize BRDF effects to a certain degree (similar to larger FOV of point spectrometers (Zhao et al., 2015)), it introduces additional uncertainty as long as it is not possible to trace which parts of which images were overlapping and thus averaged. Although an approximately uniform flying speed and along-track image overlap can be assumed, it is not guaranteed that similar parts overlapped for all areas of the scene. This might influence the retrieved spectral data, as will be seen later in Section 4.2. Within the HS DSM_{dis}, stronger angular effects are apparent in the composed scene and may influence the results of retrieval methods; however, they can still be traced based on the pixel position and included in the analysis.

Overall, these results demonstrate that differences are clearly visible between the processing modes, but their interpretation is not trivial as angular effects, the structure of the canopy and the image composition interact. Additionally, they might have a significant impact on the data

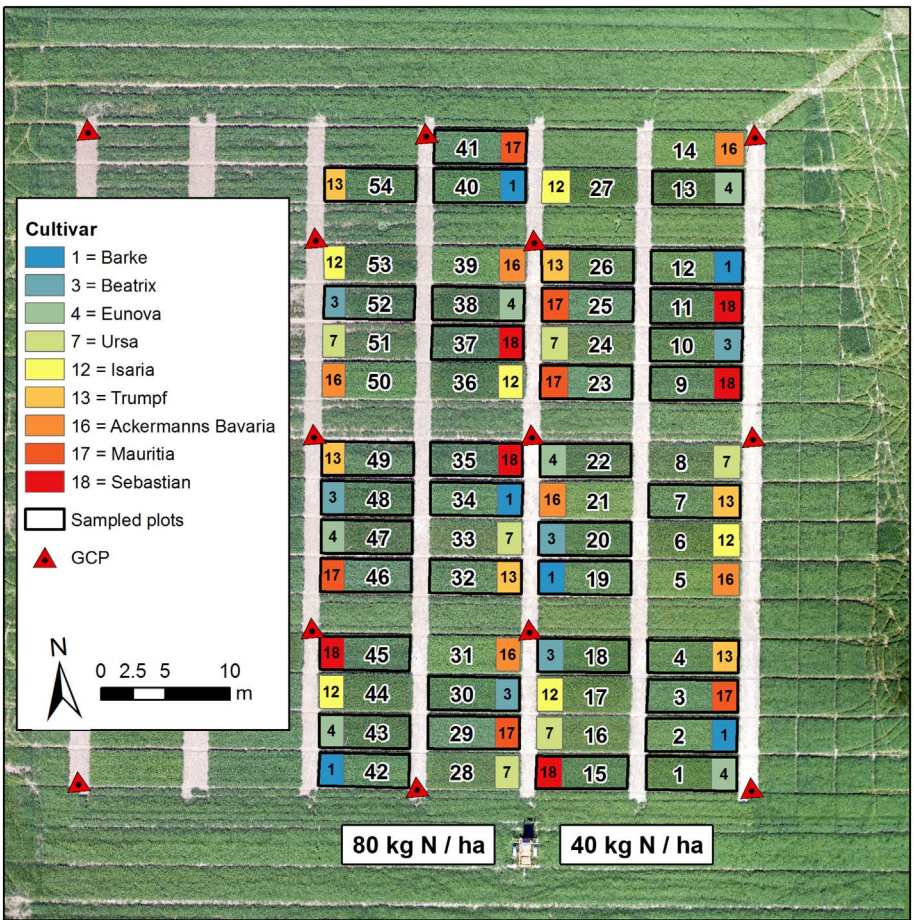


Fig. 2. RGB orthomosaic of the field experiment at 70 days after seeding. The black squares mark the experimental plots. Destructive sampling was carried out in the colored areas. The color relates to the different genotypes. (For interpretation of the references to color in this figure legend, the reader is referred to the web version of this article.)

(Modified from Aasen, 2016a).

Table 2

Formula for the vegetation indices with references used in this study. The wavelengths are slightly adapted to the available wavelength of the UHD.

VI	Formula	Reference
NDVI	$\frac{(R_{798} - R_{670})}{(R_{798} + R_{670})}$	Rouse et al. (1974)
TCARI/OSA-VI	$\frac{3 * ((R_{702} - R_{670}) - 0.2 * (R_{702} - R_{550}) * (R_{702} / R_{670}))}{1.16 * (R_{798} - R_{670}) / (R_{798} + R_{670} + 0.16)}$	Haboudane et al. (2002)
PRI	$\frac{(R_{550} - R_{530})}{(R_{550} + R_{530})}$	Gamon et al. (1992)
REIP	$700 + 40 * \frac{(R_{670} + R_{778})/2 - R_{702}}{R_{738} - R_{702}}$	Guyot et al. (1988)

product. Rasmussen et al. (2016) found that angular effects introduce variations greater than variations between different crop treatments. Currently, illumination differences resulting from different viewing geometries within an image mosaic are often ignored (Koukal et al., 2014). Additionally, the UAV trajectory might differ from flight to flight due to wind or other navigational uncertainties. Further, environmental effects such as the position of the sun might also vary between observations. Thus, pixel-wise information about the angular properties, the signal quality and the environmental conditions during the acquisition should be incorporated as a standard in the metadata for scientific grade remote sensing data. Additionally, reliable BRDF correction routines must be developed for 2D imagers. Because incorporating high-resolution structural information is seen as the way forward for these corrections (Weyermann et al., 2014) the 3D data contained within the HS DSMs are potentially suited for that use.

4.2. Influence on the specific field of view

The SFOV defines the composition of pixels and their angular properties that are used to characterize an AOI. Fig. 4 shows the FOV of the UHD (orange), FS3 (gray) and the SFOV for plot 35 at DAS 70 with the processing mode blending disabled (HS DSM_{dis}, Fig. 4C) and blending average (HS DSM_{avg}, Fig. 4D). The SFOV of the single image is marked as image 2 in Fig. 4C.

Non-imaging spectrometers such as the FS3 average the spectral signature of all objects within their FOV almost equally (Mac Arthur et al., 2012). The FOV of the UHD is composed by the individual IFOVs of every pixel. The UHD and FS3 have a similar FOV. The FS3 has a circular FOV of approximately 25°, while the UHD has rectangular FOV of approximately 20°. Thus, applied from the same height, both instruments cover a similar area. Additionally, if all pixels of the UHD were averaged, the integration of the solid angles of the IFOVs (= SFOV) would compose an FOV similar to the FS3, and therefore the angular properties of the resulting spectra would also be similar (Fig. 4B).

When the UHD is applied on a UAV, the footprint increases with as the flight altitude increases. At the same time, the AOI is covered by a smaller part of the FOV and consequently, the SFOV also changes. In an HS DSM, the AOI might be covered by multiple images (cf. Section 2). Thus, the SFOV also spans multiple images. Because the processing mode defines how the individual images are composed, it also influences the SFOV and consequently the spectral information. For the processing mode blending ‘disabled,’ only the non-overlapping parts of a few images are used. Thus, the SFOV also only uses a small part of the entire FOV of the UHD (Fig. 4A and C). When the blending mode ‘average’ is used, the information from all images that cover the AOI is used in the SFOV. Thus, a larger part of the FOV of the UHD is used. In

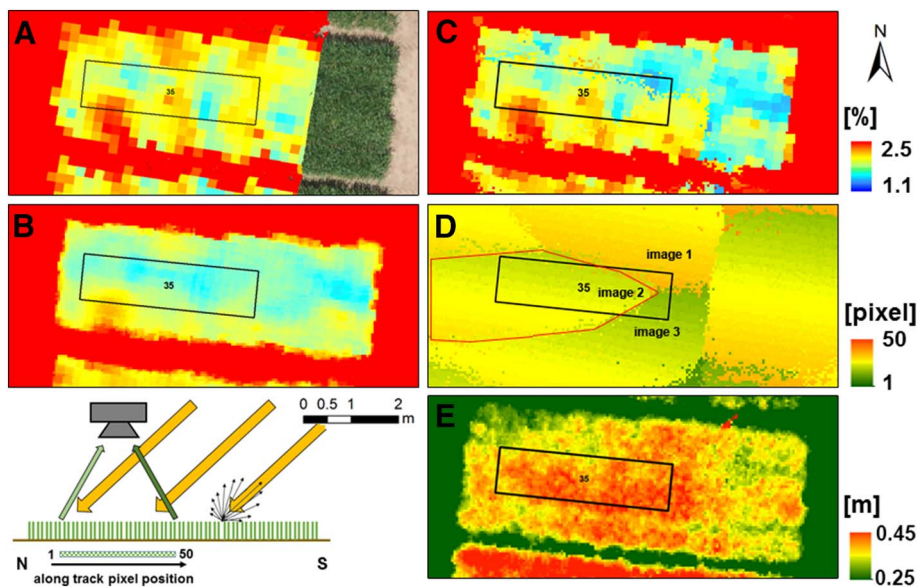


Fig. 3. Reflectance of one plot at 670 nm of plot 35 at DAS 70 as seen within a single image (A), the HS DSM_{avg} (B), the HS DSM_{dis} (C) and a visualization of the along-track pixel position within the original images used to compose the HS DSM_{dis} (D). Additionally, the plant height (E) and a schematic drawing of the relationship between the along-track pixel position and measurement geometries are shown (bottom left). (For interpretation of the references to color in this figure legend, the reader is referred to the web version of this article.)

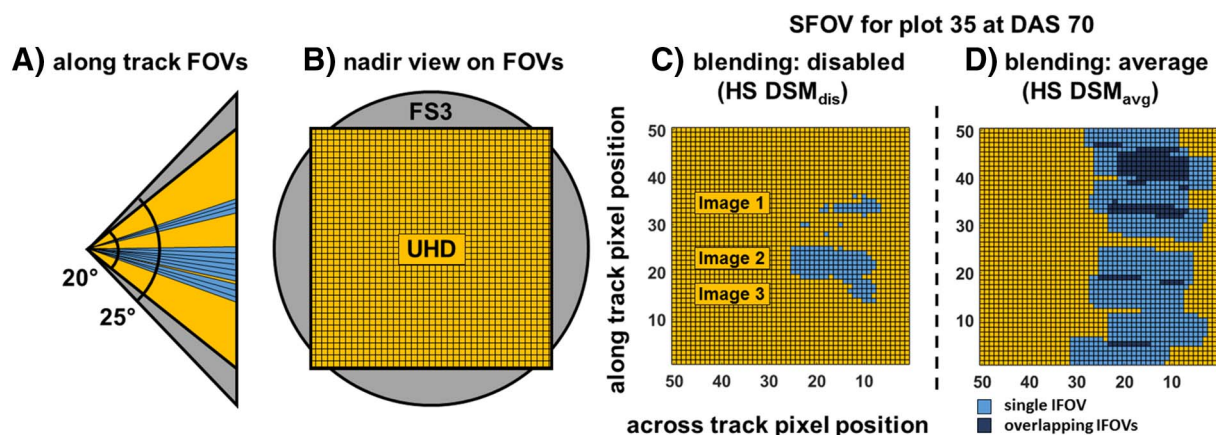


Fig. 4. Comparison of the 25° FOV of the FS3 (gray) and 20° of the UHD (orange) and their footprint from the same height (A,B). For plot 4 at DAS 70, the specific field of view (SFOV) within the hyperspectral digital surface for the processing mode 'disabled' (C) and (D) is shown in blue. Overlapping IFOVs are colored dark blue. In blending mode 'disabled,' the plot is characterized by spectral information from three images. Additionally, the resulting along-track SFOV is shown in light blue (A). In blending mode 'average,' the spectral information from nine images is taken into account and almost the entire along-track FOV of the UHD is used. (For interpretation of the references to color in this figure legend, the reader is referred to the web version of this article.)

addition, some areas of the FOV are used twice (Fig. 4D). The different composition of the SFOV also influences the spectral information.

Fig. 5 shows the spectra extracted from the two data products and the FS3 in comparison to a single nadir image. In particular, differences become visible when the spectral information is normalized to ANIF by the nadir information. The ANIF of the HS DSM_{dis}, HS DSM_{avg} and FS3 show a similar pattern. From the green to the red spectral region at 682 nm, the ANIF decreases to 0.96 and 0.89 for the HS DSM_{dis} and HS DSM_{avg}, respectively. In the red-edge, the ANIF increases before it reaches a level close to 1 in the NIR, which indicates a similar reflectance compared to the single image. The shape is most pronounced for the FS3 (ANIF = 0.83 at 682 nm), followed by the HS DSM_{avg}. While the FS3 crosses the two other ANIF curves in the red-edge and even shows an ANIF above 1 in the red-edge towards the NIR, the ANIF of HS DSM_{avg} stays below the ANIF of the HS DSM_{dis}.

To explain the difference between the different spectra from the data products and devices, the geometric composition of the SFOV of the HS DSMs and FOV of the FS3 must be investigated. In particular, the measurement geometry and size of the integrated solid angle of the SFOV interact with the illumination conditions and the canopy structure, including canopy cover.

4.2.1. Impact of canopy cover

Diffuse illumination conditions were present at DAS 56 and thus, the effects resulting from direct illumination had only a minor impact on the difference of the apparent reflectance. Still, differences also appeared under these conditions. Fig. 6 (left) shows a plot with sparse and dense vegetation and the ratio of the spectra derived from the HS DSM_{avg} and HS DSM_{dis} from these plots. The comparison of the spectra derived from the two data products reveals wavelength-dependent differences with a shape similar to those in Fig. 5. To comprehend these results, one must examine the beam geometries within the SFOVs.

The SFOVs of the single image comprises only few pixels with a measurement geometry close to nadir (Fig. 7A). The SFOV from the HS DSM_{dis} already comprises more pixels with measurement geometries further from nadir (Fig. 7B). The spectrum derived from the HS DSM_{avg} comprises even more off-nadir information as it almost uses the full 20° FOV of the UHD in the along-track direction (Fig. 7C). The integrated information of the non-imaging FS3 captures information within the full 25° FOV of the device (c.f. Fig. 4). This influences the retrieved spectrum, as shown in the data of DAS 56.

Measurements with a close-to-nadir measurement geometry have an increased proportion of soil signature compared to oblique

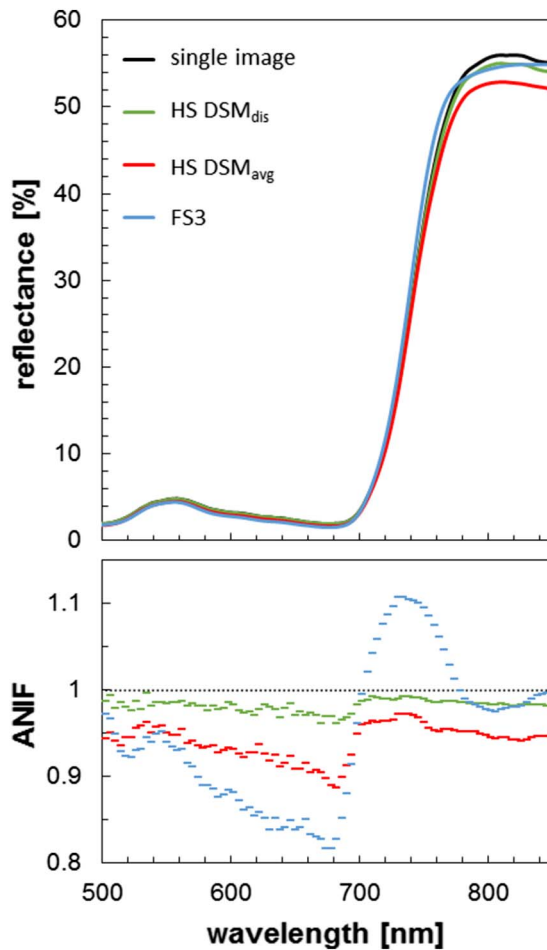


Fig. 5. Comparison of the spectra extracted from the AOI of plot 35, DAS 70 (cf. Fig. 4) from a single image (black), the HS DSM with blending mode ‘disabled’ (HS DSM_{dis}, green) and ‘average’ (HS DSM_{avg}, red) and the FS3 (blue). Additionally, anisotropy factors of the difference cases (ANIF; the reflectance normalized by the spectrum extracted from the single nadir looking image) is shown with the same color-coding (bottom). (For interpretation of the references to color in this figure legend, the reader is referred to the web version of this article.)

measurements. Compared to green vegetation, soil has a higher reflectance in the VIS and lower reflectance in NIR. Thus, measurements close to nadir have a higher reflectance in the VIS. In the red-edge region, this changes, and in the NIR, the soil influence decreases the reflectance (Burkart et al., 2015; Schaepman-Strub et al., 2006; Verrelst et al., 2008; Zhao et al., 2015).

These effects explain the general shape of the reflectance ratios seen in Fig. 6. Because the SFOV in the HS DSM_{dis} is situated around the nadir and is narrower compared to the SFOV of the data extracted from

the HS DSM_{avg}, relatively more beams from the soil are received. On the other hand, due to the wider SFOV of the HS DSM_{avg}, more beams from plant material are represented in the HS DSM_{avg} (cf. Fig. 7). The more soil signature is contained in the spectrum, the higher the reflectance in the red, lower at the NIR shoulder and the flatter the red-edge. Thus, the ratio between HS DSM_{avg} and HS DSM_{dis} is low in the red and increases towards the NIR. In denser canopies, soil signature only reaches the sensor from the most nadir beams. Thus, the spectrum extracted from the HS DSM_{avg} contains only minor soil information. Because the HS DSM_{dis} views close to nadir into the canopy, the difference between the information contained in the HS DSM_{avg} and HS DSM_{dis} increases, as seen in the ratio for plot 23 (Fig. 6).

4.2.2. Impact of measurement geometry and illumination

The influence of the measurement geometry varies with the illumination conditions and canopy structure. Fig. 8 shows the correlation between the difference of the average pixel position of the SFOV per plot of the HS DSM_{dis} and HS DSM_{avg} and the apparent reflectance for the four campaigns.

For the along-track direction, most correlations are negative. This aligns with the theory since a positive difference of the pixel position within the HS DSM_{dis} corresponds to information that has been recorded at a more acute angle to the sun (closer to the hotspot, resulting in a higher apparent reflectance) than the HS DSM_{avg} data, and vice versa. In most parts of the VIS, correlations between $0.6 < R < 0.86$ are found for the along-track pixel position for DAS 70 to 84. The strongest correlations are found at DAS 70 and decrease slightly with the growth stage. In the NIR, the correlations decrease towards the later growth stages. This results from the denser canopy in the later growth stages (and tilting of the stems due to the development of ears at DAS 96), which results in more scattering in the NIR and a decrease of BRDF effects. This aligns with modeled (Küster, 2011) and empirical (Roosjen et al., 2016) results that show that for barley in the growth stages after stem elongation, the pronouncement of BRDF in the NIR decreases. At DAS 56, a pattern different to the other DAS patterns with poor correlations is found, particularly in the VIS. At this date, cloudy diffuse illumination conditions were present, which generally reduce BRDF effects and remove their directionality to a radial gradient around the nadir resulting from the soil influence (Schaepman-Strub et al., 2006).

The correlations with the across-track pixel position are rather weak for all DAS for two reasons. First, BRDF effects are less pronounced in the direction orthogonal to the principal plane of the sun. Second, the BRDF is symmetric to the principal plane (Küster, 2011). Since the plots were aligned in this direction, the symmetry of the BRDF normalized the differences in the across-track direction.

These results, together with the results of Section 4.2.1, explain what is exemplarily shown for plot 35 at DAS 70 (cf. Fig. 5). Based on the considerations in Section 4.2.1, the apparent reflectance in the NIR in the HS DSM_{dis} and HS DSM_{avg} should have been higher than in the single image; additionally, the ANIF of the HS DSM_{avg} should have been

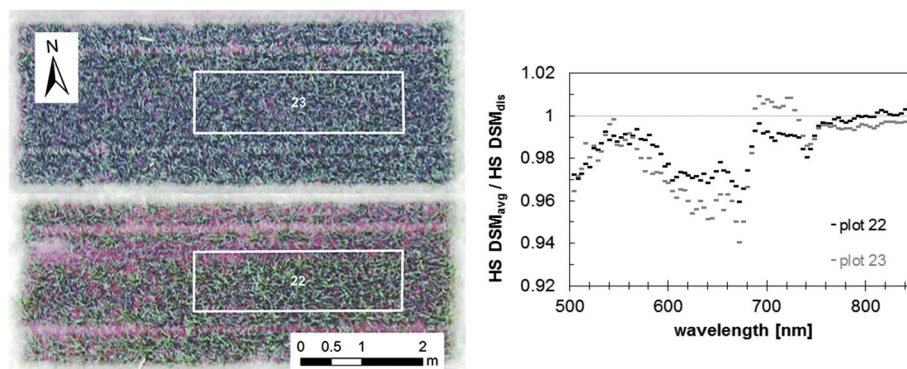


Fig. 6. RGB image of plot 22 and plot 23 (histogram stretch was applied to enhance the visible differences between soil and plants) and the ratio of the spectrum derived from the HS DSM_{dis} and HS DSM_{avg} for the two plots.

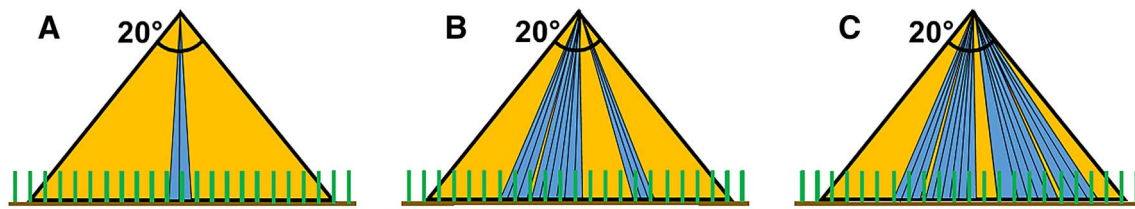


Fig. 7. Schematic drawing of the specific field of view (blue) within a single image (A), HS DSM_{dis} (B) and HS DSM_{avg} (C) in relation to the FOV of the UHD (yellow). (For interpretation of the references to color in this figure legend, the reader is referred to the web version of this article.)

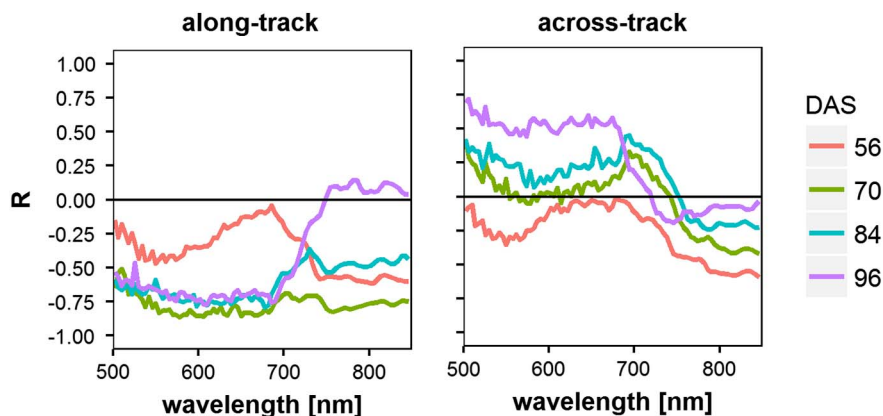


Fig. 8. Correlation (R) between the difference of the averaged along-track (left) and across-track (right) pixel position of HS DSM_{dis} and HS DSM_{avg} and the ratio of the apparent reflectance derived from both data products for the four days after seeding (DAS).

higher in the NIR than the ANIF of the HS DSM_{dis}. In combination with the distribution of the images of this plot shown in Fig. 4(D) and the impact of the measurement geometry shown in this chapter, the effects can be comprehended. The images were captured such that the along-track axis (and thus the along-track pixel position gradient) was facing north to south. During the flight at DAS 70, more images of plot 35 were captured from a sun averted measurement geometry (cf. Fig. 4D), and consequently, they contained lower apparent reflectance (for a visualization of the differences in reflectance resulting from the different measurement geometries for this particular plot, please refer to Aasen, 2016b). Because all these images are averaged in the HS DSM_{avg}, the apparent reflectance is relatively decreased in comparison with the single image and the HS DSM_{dis}.

These effects must be kept in mind when data from different sensors flown at different altitudes are compared. In comparison with high-flying platforms, the variety of viewing geometries within a SFOV of an AOI might differ considerably more in data from low-flying imaging systems, since a larger part of the FOV are used to cover the same area. This is important because it has been shown that angular effects influence the retrieval of vegetation properties (Burkart et al., 2015; Verrelst et al., 2008). In general, it can be assumed that an integration over a wider FOV or SFOV is more robust against angular effects (Zhao et al., 2015). On the other hand, well-defined angular properties offer the opportunity to derive additional information about the surface (Schaeppman, 2007). In particular, when 2D imagers capture overlapping images to derive HS DSMs, the same area is measured from multiple positions. Thus, 2D imagers provide an optimal tool for the derivation of multi-angular properties (Aasen, 2016b; Hakala et al., 2010; Honkavaara et al., 2014; Koukal et al., 2014). Future studies should exploit this opportunity. At the same time, the gained understanding should be used to further develop and adapt existing methods for the correction of angular effects (Schläpfer et al., 2015). In the future, the high-resolution 3D information contained in HS DSMs could support this correction.

Further, these results show that spectral remote sensing can also benefit from cloudy (diffuse) conditions since BRDF effects are reduced. So far, this has received little attention but it is particularly interesting in the context of UAVs since they can gather data below the clouds.

Under these conditions, however, the irradiance field is different and it has been shown that this impacts the retrieval of biophysical properties (Bartlett et al., 1998; Damm et al., 2015).

4.3. Radiometric calibration conditions

The reflectance at DAS 56 within the HS DSM shows an overall increase in reflectance compared to the field spectrometer measurements. The effects discussed so far cannot explain this difference. On this date, cloudy conditions were present. Fig. 9 shows the reflection of a reference panel under cloudy and clear sky conditions when the UAV is held above the panel by a person standing within and perpendicular to the principal plane of the sun.

Under cloudy conditions, the reflectance of the panel is reduced by approximately 14%. Depending on the cloud cover and the distance of the panel to the UAV, this value changes (not shown here). Clouds change the illumination regime from a mostly directed illumination to diffuse illumination conditions, where light is irradiated approximately

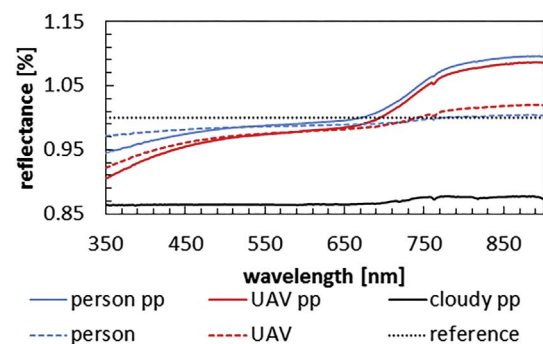


Fig. 9. Measurements of a Zenith Light reference panel under clear sky conditions (reference), with a person behind the panel in the principal plane (person pp), person perpendicular to the principal plane (person), with a UAV above the panel held by a person within the principal plane (UAV pp) and a UAV held from a person perpendicular to the principal plane (UAV). Additionally, a measurement under cloudy conditions with a UAV held by a person within the principal plane relative to a measurement under cloudy conditions without obstacles (cloudy pp).

homogeneously from the whole hemisphere. When a UAV and a person holding the UAV cover large parts of the hemisphere, the illumination of the panel is significantly reduced; so, however, is the position of the person holding the UAV. When the person holding the UAV is standing within the principal plane, the reflection in the VIS is decreased by up to 4% (at 466 nm). In the NIR, the reflectance is increased by 8.5%. When the person stands perpendicular to the principal plane, the influence is significantly reduced in the NIR to an increase of only 1.9% compared to the case without obstacles. In the VIS, it is slightly reduced to 3.4%. The presence of the UAV only changes the influence slightly. When the person stands in the principal plane, the UAV even reduces the difference in the pure reflectance of the reference panel. Similar to the clouded case, the decrease in the VIS can be attributed to the covering of the hemisphere. Because the hemisphere mostly scatters blue light under clear sky conditions, the decrease is most pronounced in this region. As the UAV increases the covered area, the influence is increased. In the NIR, the person and the UAV are scattering light back on the panel. Thus, at approximately 670 nm, the reflectance increased. The slight difference of approximately 1% in the NIR between the case with and without the UAV is most likely explained due to slight differences in the distance to the panel. Similar results are found by Kimes et al. (1983), who reported errors from 2 to 18% in field spectrometer measurements depending on the distance and position of a person close to a reference and the color of the clothing worn by the operator.

The pre-flight calibration procedure used in this study is a commonly used one in UAV remote sensing and field spectroscopy. The demonstrated calibration issue has great implications for the data quality. Since the measurement of the reference panel is used to transform all image cubes to reflectance, errors will propagate into every measurement. Worse, this error cannot be quantified afterwards. Therefore, data calibrated with this approach cannot be directly compared to data captured under different illumination conditions, as will be seen in Section 4.4 for DAS 56. On the other hand, within one campaign, the data stay consistent because an eventual offset influences all measurements. Consequently, the issue does not affect most of the results of this study. Due to the knowledge of these effects, the greatest care was taken to minimize their impact during the calibration procedure. Additionally, both the HS DSM_{dis} and HS DSM_{avg} would be affected in the same way. Thus, the results of the comparison between both data products are not affected by this issue. Still, since the FS3 measurements have been calibrated separately and (as in every other study) the same issue might bias them, the comparison to the UHD data (Fig. 5) is afflicted by some uncertainty.

In the future, this calibration method should be avoided. For UAVs, robust methods based on laboratory calibrations, characterized ground targets (e.g., Lucieer et al., 2014b), and the ability to adapt to changing illumination conditions (e.g., Burkart et al., 2015) are necessary to derive more robust scientific grade data. This is particularly important when multi-temporal surveys under different illumination conditions are carried out; however, sensing systems are needed that can record the incident radiation.

4.4. Comparison to proximal non-imaging and destructive ground measurements

The previous sections outlined systematic differences between data captured by imaging and non-imaging devices as well as the influence of different processing modes. In the following sections, the impacts of these differences are shown for the entire set of case study data.

Fig. 10 shows maps of the REIP for DAS 56 to 96 calculated from the HS DSM_{dis}. For all dates, differences between different cultivars and fertilizer levels and within plots can be seen. For DAS 70 to 96, the differences between the cultivars become more pronounced. Additionally, in some plots, the positions of the destructive measurements from the previous dates can be identified (e.g., square with low REIP value in the destructive measurement part of plot 10 at DAS 70) as well

as crop damage due to rabbit burrows (DAS 70, in the middle of the plot south to plot 54). In DAS 96, the lodging of some plots is visible due to very low REIP values (unmarked plots 6, 17, 27, 36, 44, 53).

The effects resulting from the data processing, however, can also be seen. In DAS 84, the influence of the transition of the images of two flight lines is apparent in the second row from the west, while most other transitions are not as obvious. Here, the images are shifted for approximately half an image in the along-track direction. Thus, the measurement geometries of adjacent pixels are different and BRDF effects become visible (cf. Sections 4.1 and 4.2). Similarly, in plot 4, 35 and between plot 30 and 32 at DAS 70, edges are visible within the plots and can be explained by the same phenomenon. At DAS 56, the low REIP values cannot be explained by plant physiological reasons or by data processing. Here, the bias of the calibration procedure (cf. Section 4.3) under cloudy conditions becomes visible. In the following section, the imaging data are compared to non-imaging spectral ground measurements.

4.4.1. Non-imaging spectral ground measurements

In coordination with UAV overflights, non-imaging FS3 measurements were taken. Fig. 11 shows the coefficient of determination of FS3 and HS DSM_{dis} data (A) and the slope of the relationship (B). The scatterplots for six exemplary wavelengths can be found in the appendix (Fig. A.1). Additionally, Fig. 11 shows scatterplots of the four VIs NDVI (C), TCARI/OSAVI (D), REIP (E) and PRI (F) retrieved from the FS3 and HS DSM_{dis} data.

In the VIS domain, the spectral information from the FS3 and HS DSM_{dis} are well correlated at DAS 84 and 96. At DAS 70, the correlations are weaker but still highly significant ($p < 0.001$). In the NIR domain, the correlations are lower. For DAS 84 and 96, they are still highly significant ($p < 0.001$) and for DAS 70, the correlations are lower and less significant ($p < 0.07$).

At DAS 70, the measurements of the FS3 were carried out two days after the UHD overflights. On this day, slight, fast-changing cirrus clouds were present that can affect the spectral measurements and lower the correlations between the datasets. The general decrease in the correlation in the NIR can be explained by the bidirectional reflectance function of barley. In the VIS (at 670 nm), the reflectance is almost linearly decreasing from the hotspot to the nadir along the principal plane (Küster, 2011, Appendix), while in the NIR (at 800 nm), there is variation around nadir. Thus, the different SFOVs of the FS3 and HS DSM_{dis} have a lower impact in the VIS than in the NIR. The differences between the VIS and NIR also result in different slopes of the relationship (Fig. 11B). A similar slope for the VIS and NIR domain is only found at DAS 96, where ears had already emerged and were tilted above the canopy, and the plants were already in the process of senescence, which reduced the impact of the different SFOV compositions.

For DAS 56, significant ($p < 0.05$) correlations are only found in the NIR. The correlations were most likely affected by the fluctuations in incident radiation between calibrations and measurements. Due to the small differences in reflectance in the VIS, this affects the VIS more than the NIR due to the larger absolute differences in reflectance between the plots in the NIR. Because several non-traceable influences interacted at DAS 56, the results of the comparison of the FS3 and HS DSM data must still be handled with care at this date.

The wavelength depended differences between the imaging and non-imaging data also impact the VIs (Fig. 11, Table 3). For most DAS, the NDVI is lower for the HS DSM_{dis} data. Here, the higher proportion of soil in the HS DSM_{dis} signal decreases the VI values. At DAS 96, the FS3 measurements were carried out six days later than the UHD measurements. Thus, the advanced senescence at the time reduced the NDVI values of the FS3. For DAS 56, the NDVI is the only VI that can compensate for the calibration bias.

For the REIP, the relationships between the FS3 and HS DSM_{dis} are similar for all DAS but DAS 56. The higher REIP values derived from HS

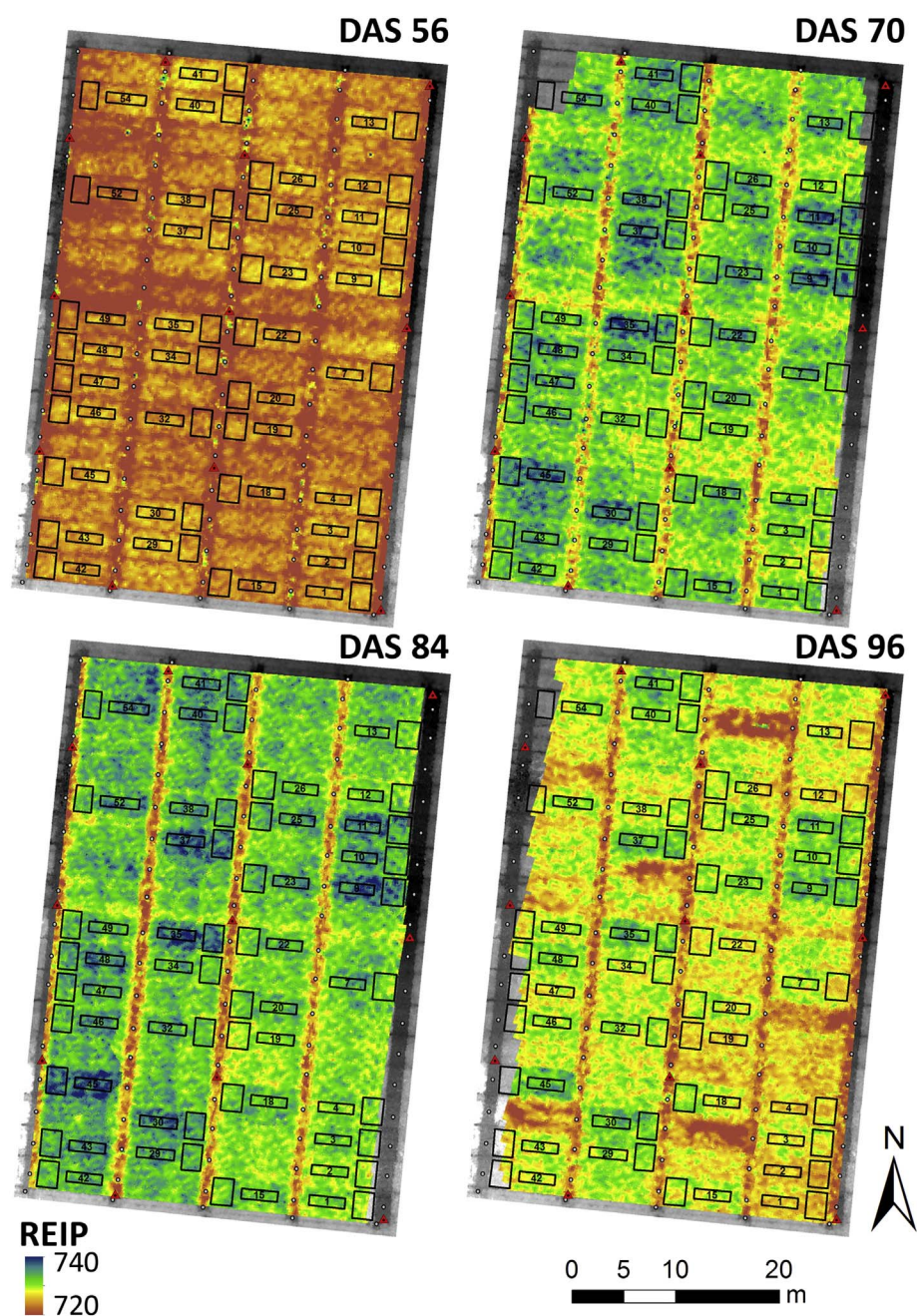


Fig. 10. Maps of the red-edge inflection point (REIP) derived from the hyperspectral digital surface model of DAS 56, 70, 84 and 96. Please note that the data for DAS 56 are biased by the calibration under cloudy conditions (cf. Section 4.3). (For interpretation of the references to color in this figure legend, the reader is referred to the web version of this article.)

DSM_{dis} data can be explained by the lower proportion of plant signatures in the HS DSM data due to the different viewing geometries within the SFOVs. At DAS 56, the relative overestimation of the reflectance due to the calibration bias of the UHD (c.f. Section 4.3) increases the absolute reflectance in higher wavelengths more than in lower wavelengths. Thus, the slope between the red and NIR increases and the REIP decreases.

For the TCARI/OSAVI, the FS3 values are higher than those from the HS DSM_{dis} for DAS 70 to 96. Because the TCARI/OSAVI is sensitive to chlorophyll content (Haboudane et al., 2002), this can also be explained by the lower proportion of plant signatures in the HS DSM_{dis} data compared to the FS3 data.

The relationships between the FS3 and HS DSM_{dis} PRI differ for each DAS and show low R^2 . The two wavelengths used in the PRI (550, 530) have different sensitivities to a changing SFOV (c.f. Fig. 5) and vegetation cover (c.f. Fig. 6). Thus, the PRI is very sensitive to differences in the SFOV and reacts differently in different growth stages.

Differences in the data acquired from the same area but with different sensors have been found earlier; however, this was mostly attributed to non-sufficient (cross-) calibrations of the sensing system (Bareth et al., 2015; von Bueren et al., 2015). The results of this study suggest that these differences also result from the different angular properties of the data used to characterize an AOI (= SFOV) and that this influence is wavelength and growth stage dependent.

4.4.2. Destructive chlorophyll measurements

In Table 4, the coefficient of determination for the estimation of chlorophyll with different VIs from the data of the HS DSMs and the FS3 is shown. For DAS 56 and 70, low R^2 are found for both the UHD and the FS3 data. In addition to the biased calibration of the UHD, this may be caused by the different illumination conditions at DAS 56, which also affects the retrieval of biophysical properties (Bartlett et al., 1998; Damm et al., 2015). For DAS 84 and 96, R^2 between 0.41 and 0.61 are found with the REIP and an R^2 of approximately 0.50 is achieved with

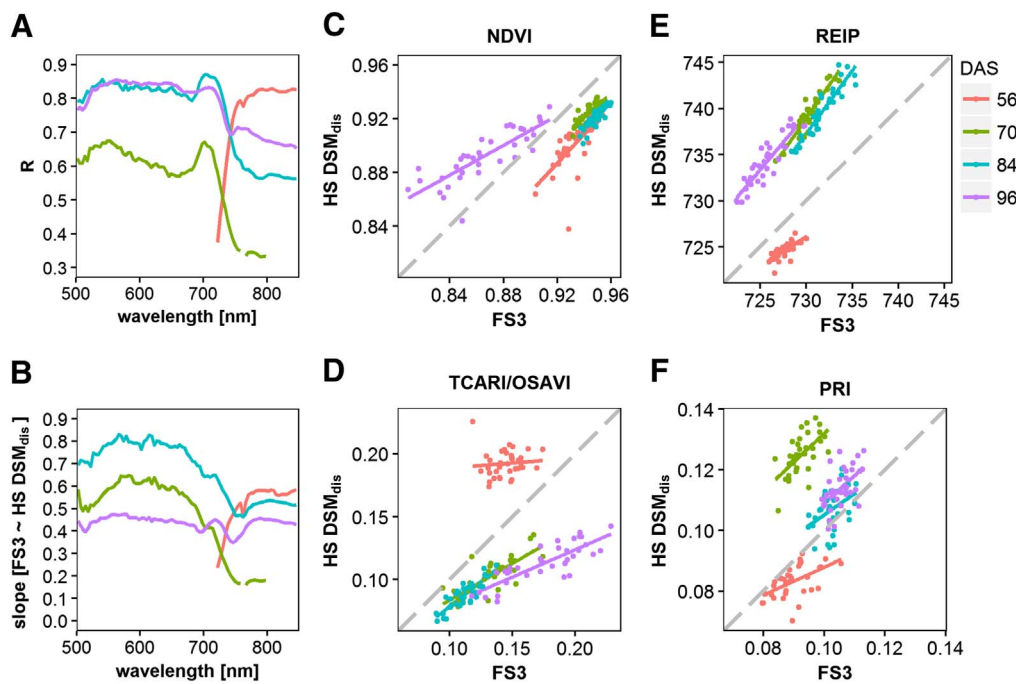


Fig. 11. Correlation coefficient (A) and the slope (B) for all significant ($p < 0.05$) relationships of the FS3 and HS DSM_{dis} data for the different days after seeding (DAS). Additionally, scatterplots of the vegetation indices NDVI (C), TCARI/OSAVI (D), REIP (E) and PRI (F) are shown.

Table 3

Slope and coefficient of determination between the vegetation indices calculated from the HS DSM_{dis} and FS3 data.

DAS	NDVI		TCARI/OSAVI		PRI		REIP	
	slope	R ²	slope	R ²	slope	R ²	slope	R ²
56	1.07	0.46	0.08	0.01	0.46	0.28	0.63	0.53
70	0.87	0.65	0.58	0.64	0.94	0.36	1.45	0.87
84	1.05	0.73	0.79	0.74	0.70	0.17	1.37	0.86
96	0.56	0.68	0.44	0.70	0.92	0.31	1.19	0.82

Table 4

Coefficients of determination (R²) of different vegetation indices for the prediction of chlorophyll for the individual dates and across the DAS 70–96 and 84–96 from the HS DSM_{dis}, HS DSM_{avg} and FS3 data.

DAS		56	70	84	96	70–96	84–96
NDVI	HS DSM _{dis}	0.00	0.02	0.14	0.55	0.42	0.52
	HS DSM _{avg}	0.00	0.03	0.12	0.58	0.42	0.52
	FS3	0.00	0.00	0.00	0.27	0.34	0.40
TCARI/OSAVI	HS DSM _{dis}	0.00	0.09	0.27	0.44	0.36	0.54
	HS DSM _{avg}	0.00	0.11	0.23	0.44	0.35	0.52
	FS3	0.00	0.09	0.10	0.23	0.42	0.37
PRI	HS DSM _{dis}	0.30	0.04	0.16	0.14	0.10	0.29
	HS DSM _{avg}	0.34	0.15	0.22	0.18	0.11	0.44
	FS3	0.10	0.34	0.31	0.31	0.20	0.41
REIP	HS DSM _{dis}	0.18	0.20	0.44	0.60	0.57	0.66
	HS DSM _{avg}	0.15	0.23	0.41	0.61	0.57	0.65
	FS3	0.13	0.27	0.30	0.49	0.53	0.57

TCARI/OSAVI for both the HS DSM and FS3 data. Additionally, in the combined data of DAS 70–96 and 84–96, the REIP from the HS DSM data yielded R² values between 0.57 and 0.66. Although the R² values are comparable to other studies for single and multi-temporal studies using VIs (Quemada et al., 2014; Yu et al., 2014), several remarks can be given. In Fig. 10 it is apparent that the experimental plots are not homogenous. Thus, the chlorophyll values estimated on individual leaves at the destructive part of the plot do not necessarily reflect the average chlorophyll value of the plot. In the future, destructive field measurements should be precisely georeferenced to enable a

comparison with imaging spectroscopy data—particularly for very-high-resolution data such as UAV data.

The results from the HS DSM_{dis} and HS DSM_{avg} differ slightly in most cases. The results of the FS3 and HS DSM data differ significantly in most cases. Interestingly, in most cases, the VIs calculated with the HS DSM data performed better than the VIs calculated from the FS3 data. Originally, the REIP and TCARI/OSAVI were developed from modeled data. Although not clearly stated in the original papers (Guyot and Baret, 1988; Haboudane et al., 2002), the VIs might have been developed for a more directional nadir looking narrow FOV case. Thus, the angular properties present in HS DSM data might be better suited for parameter retrieval with those VIs. On the other hand, PRI was developed with data of a spectrometer with an FOV of 15° (Gamon et al., 1992) and in most cases showed better performance for FS3 data. These results highlight that caution must be taken when results from one sensor are compared to results from different sensors or processing schemes.

5. Conclusion

Low-flying sensing systems can carry out surveys efficiently without disrupting the surface. In combination with 2D spectral imagers, spectral and 3D spatial information can be captured simultaneously and at very high resolution. Besides of the recent developments in multi-spectral LIDAR systems (Suomalainen et al., 2011), 2D imaging spectroscopy is currently the only technique that allows the derivation of spectral and 3D data at the same time with the same sensor (Aasen et al., 2015). With data products such as high-resolution hyperspectral digital surface models, precision agriculture or field-phenotyping applications can be supported. In comparison with non-imaging observations, where only a limited amount of measurements can be carried out, hundreds of pixels are captured from an AOI. This allows the detection of small-scale variability within the canopy such as animal damage, lodging or tractor tracks. Future studies could further exploit these data by applying pixel-wise methods and zonal statistics that would also represent the variety within a certain area. In order to fully comprehend the data, however, one must consider its properties.

Imaging spectroscopy with 2D imagers generates a spectral representation of a scene by recording multiple overlapping images, which are composed to create the full scene based on a particular

processing scheme. In this study, the theoretical framework to understand the data properties of these scenes was developed. Every pixel in an image has its own measurement geometry, which influences the apparent spectral reflectance because it interacts with the canopy anisotropy and illumination conditions. As a result, the data contain BRDF effects. The data processing scheme defines how this spectral information is composed and thus defines the angular properties of the pixels in the resulting scene. Depending on the processing scheme used, the data might differ.

- The concept of the specific field of view (SFOV) describes the composition of pixels and their angular properties within a scene used to characterize a specific AOI on the ground. It allows understanding the complex composition of the signal extracted from a data product.
- When the spectral information is extracted from a scene where no blending of the spectral data is applied (HS DSM_{dis}), the SFOVs of an AOI mostly consist of pixels captured in a geometry close to the nadir, since only the central part of the images is used. Thus, the proportion of soil signature is increased and BRDF effects are more pronounced and visible in comparison with other processing modes.
- When spectral information is extracted from a scene where multiple images are averaged (HS DSM_{avg}), the SFOVs uses pixels that were captured within a large part of the FOV of the device. Thus, the proportion of off-nadir information—and consequently of plant signature—is increased in comparison to the HS DSM_{dis}. In addition, the spatial pattern of the spectral data appears smoother and BRDF effects might be normalized to a certain degree. Still, the measurement geometry within individual images affects the spectral data.
- For non-imaging data, the SFOV equals the FOV. Thus, the SFOV of data from field spectrometers is composed of a wide range of measurement geometries—in the case of the FS3, without fore optics 25° around the nadir. Thus, the proportion of off-nadir information is high.
- The differences between different processing modes and devices are wavelength-dependent. Because they result from the interaction of illumination conditions and viewing geometry, as well as canopy structure, they are also growth stage dependent. The largest relative differences are found in the red, the lowest in the NIR. In comparison to a spectrum extracted from a nadir image of a barley canopy at the booting stage, the spectral information at 682 nm of the HS DSM_{dis}, HS DSM_{avg} and of a non-imaging spectrometer differed by up to 4, 11 and 17%, respectively.
- The results show that data from imaging and non-imaging are not comparable per se. This aligns with earlier studies. This study identifies the different SFOVs as the reason for these differences. Furthermore, the retrieval of biophysical plant parameters with vegetation indices (NDVI, REIP, PRI, TCARI/OSAVI) is also influenced. Thus, caution must be taken when results from one sensor are compared to results from a different sensor or processing scheme. Further research is needed to investigate the sensitivity of different retrieval methods to different SFOVs.
- The results of this study are relevant in all cases where data captured with different SFOVs are compared. Thus they apply to every case where different sensors or different processing methods are used.

From these results, several recommendations can be given for future multi-temporal missions and necessary developments in the field of imaging spectroscopy with 2D imagers:

- Smaller spaces between image capturing positions increase the chance that information is available with a desired measurement geometry.
- The measurement geometry has a weaker influence under cloudy conditions. Additionally, low-altitude imaging spectroscopy can be carried out under cloudy conditions. This option should be further investigated; however, this requires radiometric calibration procedures that allow constant adaption to illumination.
- Reliable algorithms to correct for BRDF effects in spectral data must be developed and made available to the community. This is particularly important for low-altitude sensing systems since wider FOVs are needed to cover larger areas in the same time as high-altitude systems. The 3D information generated during the generation of HS DSMs could be used to derive structural data to support these algorithms.

With the anticipated democratization of imaging spectroscopy, the field will become more complex. When data are no longer only generated in a standardized way by experts from established space or airborne missions, the democratization of knowledge about data acquisition and processing will also be needed. This study shows that information about the angular properties of the pixels in a data product and the processing workflow should become a standard along with other quality assurance information. In general, with the diversity of sensors and processing schemes, generating and disclosing metadata about the sensor as well as the processing pipeline will be critically important to ensure comparability between results.

Acknowledgements

We sincerely thank Martin Gynp, Jonas Brands, Simon Bennertz, Janis Broscheit, Markus Drahs, Silas Eichfuss, Sven Ortloff and Maximilian Willkomm for their outstanding engagement in the field, and the people of Campus Klein-Altendorf (University of Bonn) for maintaining the field experiment. Additionally, we thank Georg Bareth and Nora Tilly for their support during the preparation of the manuscript. We also thank Ira Kurth and Maurício Hunsche (INRES, University of Bonn) for the access to and their support in the laboratory. The field measurements were carried out within CROP.SENSE.net project in the context of the Ziel 2-Programms NRW 2007–2013 “Regionale Wettbewerbsfähigkeit und Beschäftigung” by the Ministry for Innovation, Science and Research (MIWF) of the state North Rhine Westphalia (NRW) and European Union Funds for regional development (EFRE) (005-1103-0018). We acknowledge Agim Ballvora for the management of the barley cluster within this project. H. A. acknowledges the funding through the fellowship grant of the Graduate School of Geosciences (GSGS-2015B-F01), University of Cologne. We also would like to thank the three anonymous reviewers for their valuable comments that helped to improve the manuscript.

Appendix A

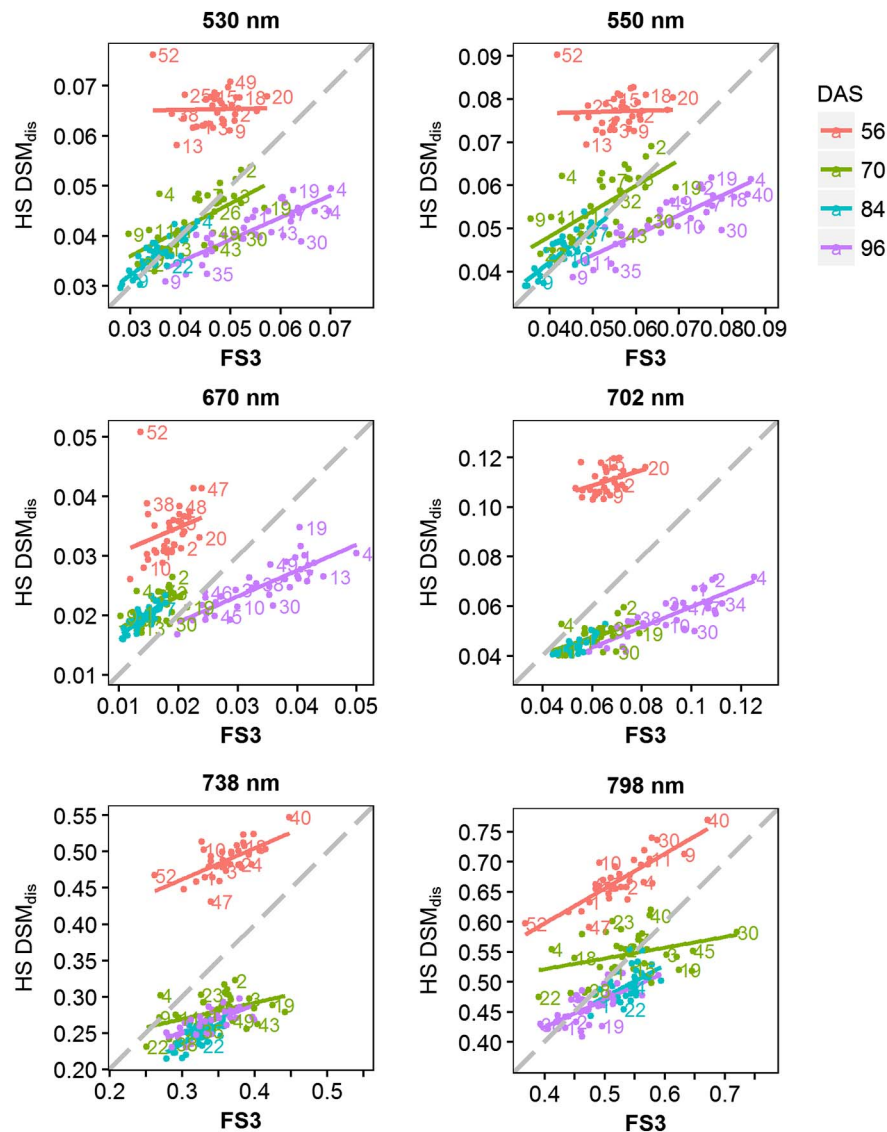


Fig. A.1. Scatterplots of the reflectance at six wavelength derived from the FS3 and HS DSM_{dis} for all plots (plot numbers are indicated with numbers)

References

- Aasen, H., 2016a. The Acquisition of Hyperspectral Digital Surface Models of Crops from UAV Snapshot Cameras (Dissertation). University of Cologne, Cologne, Germany.
- Aasen, H., 2016b. Influence of the viewing geometry on hyperspectral data retrieved from UAV snapshot cameras, in: ISPRS Annals of the Photogrammetry, Remote Sensing and Spatial Information Sciences. In: Presented at the XXIII congress of the International Society for Photogrammetry and Remote Sensing, Prague, Czech Republic.
- Aasen, H., Gnyp, M.L., Miao, Y., Bareth, G., 2014. Automated hyperspectral vegetation index retrieval from multiple correlation matrices with HyperCor. *Photogramm. Eng. Remote. Sens.* 80, 785–795. <http://dx.doi.org/10.14358/PERS.80.8.785>.
- Aasen, H., Burkart, A., Bolten, A., Bareth, G., 2015. Generating 3D hyperspectral information with lightweight UAV snapshot cameras for vegetation monitoring: from camera calibration to quality assurance. *ISPRS J. Photogramm. Remote Sens.* 108, 245–259. <http://dx.doi.org/10.1016/j.isprsjrs.2015.08.002>.
- Araus, J.L., Cairns, J.E., 2014. Field high-throughput phenotyping: the new crop breeding frontier. *Trends Plant Sci.* 19, 52–61. <http://dx.doi.org/10.1016/j.tplants.2013.09.008>.
- Bareth, G., Aasen, H., Bendig, J., Gnyp, M.L., Bolten, A., Jung, A., Michels, R., Soukka, M., 2015. Low-weight and UAV-based hyperspectral full-frame cameras for monitoring crops: spectral comparison with portable Spectroradiometer measurements. *Photogramm. Fernerkund. Geoinformation* 2015, 69–79. <http://dx.doi.org/10.1127/pfg/2015/0256>.
- Bartlett, J.S., Ciotti, Á.M., Davis, R.F., Cullen, J.J., 1998. The spectral effects of clouds on solar irradiance. *J. Geophys. Res.* 103, 31017. <http://dx.doi.org/10.1029/1998JC900002>.
- Bendig, J., Yu, K., Aasen, H., Bolten, A., Bennertz, S., Broscheit, J., Gnyp, M.L., Bareth, G., 2015. Combining UAV-based plant height from crop surface models, visible, and near infrared vegetation indices for biomass monitoring in barley. *Int. J. Appl. Earth Obs. Geoinf.* 39, 79–87. <http://dx.doi.org/10.1016/j.jag.2015.02.012>.
- Berni, J., Zarco-Tejada, P.J., Suarez, L., Fereres, E., 2009. Thermal and narrowband multispectral remote sensing for vegetation monitoring from an unmanned aerial vehicle. *IEEE Trans. Geosci. Remote Sens.* 47, 722–738. <http://dx.doi.org/10.1109/TGRS.2008.2010457>.
- Blanke, M., 1992. Determination of chlorophyll using DMSO. *Wein Wiss* 47, 32–35.
- von Bueren, S.K., Burkart, A., Hueni, A., Rascher, U., Tuohy, M.P., Yule, I.J., 2015. Deploying four optical UAV-based sensors over grassland: challenges and limitations. *Biogeosciences* 12, 163–175. <http://dx.doi.org/10.5194/bg-12-163-2015>.
- Burkart, A., Aasen, H., Alonso, L., Menz, G., Bareth, G., Rascher, U., 2015. Angular dependency of hyperspectral measurements over wheat characterized by a novel UAV based goniometer. *Remote Sens.* 7, 725–746. <http://dx.doi.org/10.3390/rs70100725>.
- Calderón, R., Navas-Cortés, J.A., Lucena, C., Zarco-Tejada, P.J., 2013. High-resolution airborne hyperspectral and thermal imagery for early detection of Verticillium wilt of olive using fluorescence, temperature and narrow-band spectral indices. *Remote Sens. Environ.* 139, 231–245. <http://dx.doi.org/10.1016/j.rse.2013.07.031>.
- Colomina, I., Molina, P., 2014. Unmanned aerial systems for photogrammetry and remote sensing: a review. *ISPRS J. Photogramm. Remote Sens.* 92, 79–97. <http://dx.doi.org/10.1016/j.isprsjrs.2014.07.001>.

- 10.1016/j.isprsjprs.2014.02.013.
- Core Team, R., 2016. R: A Language and Environment for Statistical Computing. R Foundation for Statistical Computing, Vienna, Austria.
- Damm, A., Guanter, L., Verhoef, W., Schläpfer, D., Garbari, S., Schaepman, M.E., 2015. Impact of varying irradiance on vegetation indices and chlorophyll fluorescence derived from spectroscopy data. *Remote Sens. Environ.* 156, 202–215. <http://dx.doi.org/10.1016/j.rse.2014.09.031>.
- Dandois, J.P., Ellis, E.C., 2010. Remote sensing of vegetation structure using computer vision. *Remote Sens.* 2, 1157–1176. <http://dx.doi.org/10.3390/rs2041157>.
- Domingues Franceschini, M., Bartholomeus, H., van Apeldoorn, D., Suomalainen, J., Kooistra, L., 2017. Intercomparison of unmanned aerial vehicle and ground-based narrow band spectrometers applied to crop trait monitoring in organic potato production. *Sensors* 17, 1428. <http://dx.doi.org/10.3390/s17061428>.
- Fiorani, F., Schurr, U., 2013. Future scenarios for plant phenotyping. *Annu. Rev. Plant Biol.* 64, 267–291. <http://dx.doi.org/10.1146/annurev-arplant-050312-120137>.
- Gamon, J.A., Peñuelas, J., Field, C.B., 1992. A narrow-waveband spectral index that tracks diurnal changes in photosynthetic efficiency. *Remote Sens. Environ.* 41, 35–44. [http://dx.doi.org/10.1016/0034-4257\(92\)90059-S](http://dx.doi.org/10.1016/0034-4257(92)90059-S).
- Geipel, J., Link, J., Claupein, W., 2014. Combined spectral and spatial modeling of corn yield based on aerial images and crop surface models acquired with an unmanned aircraft system. *Remote Sens.* 6, 10335–10355. <http://dx.doi.org/10.3390/rs61110335>.
- Gitelson, A., Merzlyak, M.N., 1994. Quantitative estimation of chlorophyll-a using reflectance spectra: experiments with autumn chestnut and maple leaves. *J. Photochem. Photobiol. B* 22, 247–252. [http://dx.doi.org/10.1016/1011-1344\(93\)06963-4](http://dx.doi.org/10.1016/1011-1344(93)06963-4).
- Gnyp, M.L., Yu, K., Aasen, H., Yao, Y., Huang, S., Miao, Y., Bareth, G., 2013. Analysis of crop reflectance for estimating biomass in rice canopies at different phenological stages. *Photogramm. Fernerkund. Geoinformation* 2013, 351–365. <http://dx.doi.org/10.1127/1432-8364/2013/0182>.
- Goetz, A.F.H., 2009. Three decades of hyperspectral remote sensing of the Earth: a personal view. *Remote Sens. Environ.* 113, S5–S16. <http://dx.doi.org/10.1016/j.rse.2007.12.014>.
- Goetz, A.F.H., Vane, G., Solomon, J.E., Rock, B.N., 1985. Imaging spectrometry for Earth remote sensing. *Science* 228, 1147–1153. <http://dx.doi.org/10.1126/science.228.4704.1147>.
- Guyot, N., Baret, F., 1988. Utilisation de la haute resolution spectrale pour suivre l'état des couverts végétaux. In: *Proceedings of the 4th International Colloquium on Spectral Signatures of Objects in Remote Sensing*. Presented at the 4th International Colloquium on Spectral Signatures of Objects in Remote Sensing, NASA Astrophysics Data System, Aussois, France, pp. 279–286.
- Guyot, G., Baret, F., Major, D., 1988. High spectral resolution: determination of spectral shifts between the red and the near infrared. *Int. Arch. Photogramm. Remote Sens.* 11, 750–760.
- Haboudane, D., Miller, J.R., Tremblay, N., Zarco-Tejada, P.J., Dextraze, L., 2002. Integrated narrow-band vegetation indices for prediction of crop chlorophyll content for application to precision agriculture. *Remote Sens. Environ.* 81, 416–426.
- Haboudane, D., Miller, J.R., Pattey, E., Zarco-Tejada, P.J., Strachan, I.B., 2004. Hyperspectral vegetation indices and novel algorithms for predicting green LAI of crop canopies: modeling and validation in the context of precision agriculture. *Remote Sens. Environ.* 90, 337–352. <http://dx.doi.org/10.1016/j.rse.2003.12.013>.
- Hakala, T., Suomalainen, J., Peltoniemi, J.I., 2010. Acquisition of bidirectional reflectance factor dataset using a micro unmanned aerial vehicle and a consumer camera. *Remote Sens.* 2, 819–832. <http://dx.doi.org/10.3390/rs2030819>.
- Hansen, P.M., Schjoerring, J.K., 2003. Reflectance measurement of canopy biomass and nitrogen status in wheat crops using normalized difference vegetation indices and partial least squares regression. *Remote Sens. Environ.* 86, 542–553. [http://dx.doi.org/10.1016/S0034-4257\(03\)00131-7](http://dx.doi.org/10.1016/S0034-4257(03)00131-7).
- Honkavaara, E., Arbiol, R., Markelin, L., Martinez, L., Cramer, M., Bovet, S., Chandelier, L., Iives, R., Klonus, S., Marshal, P., Schläpfer, D., Tabor, M., Thom, C., Veje, N., 2009. Digital airborne photogrammetry—a new tool for quantitative remote sensing?—a state-of-the-art review on radiometric aspects of digital photogrammetric images. *Remote Sens.* 1, 577–605. <http://dx.doi.org/10.3390/rs1030577>.
- Honkavaara, E., Saari, H., Kaivosoja, J., Pölonen, I., Hakala, T., Litkey, P., Mäkinen, J., Pesonen, L., 2013. Processing and assessment of spectrometric, stereoscopic imagery collected using a lightweight UAV spectral camera for precision agriculture. *Remote Sens.* 5, 5006–5039. <http://dx.doi.org/10.3390/rs5105006>.
- Honkavaara, E., Markelin, L., Hakala, T., Peltoniemi, J.I., 2014. The metrology of directional, spectral reflectance factor measurements based on area format imaging by UAVs. *Photogramm. Fernerkund. Geoinformation* 2014, 175–188. <http://dx.doi.org/10.1127/1432-8364/2014/0218>.
- Hueni, A., Damm, A., Kneubühler, M., Schlapfer, D., Schaepman, M.E., 2016. Field and airborne spectroscopy cross validation—some considerations. *IEEE J. Sel. Top. Appl. Earth Obs. Remote Sens.* 1–19. <http://dx.doi.org/10.1109/JSTARS.2016.2593984>.
- Jakob, S., Zimmermann, R., Gloaguen, R., 2017. The need for accurate geometric and radiometric corrections of drone-borne hyperspectral data for mineral exploration: MEPhySTo—A toolbox for pre-processing drone-borne hyperspectral data. *Remote Sens.* 9, 88. <http://dx.doi.org/10.3390/rs9010088>.
- Kimes, D.S., Kirchner, J.A., Newcomb, W.W., 1983. Spectral radiance errors in remote sensing ground studies due to nearby objects. *Appl. Opt.* 22, 8. <http://dx.doi.org/10.1364/AO.22.000008>.
- Koukal, T., Atzberger, C., Schneider, W., 2014. Evaluation of semi-empirical BRDF models inverted against multi-angle data from a digital airborne frame camera for enhancing forest type classification. *Remote Sens. Environ.* 151, 27–43. <http://dx.doi.org/10.1016/j.rse.2013.12.014>.
- Küster, T., 2011. Modellierung von Getreidebestandsspektren zur Korrektur BRDF-bedingter Einflüsse auf Vegetationsindizes im Rahmen der EnMAP-Mission. Humboldt-Universität zu Berlin, Berlin.
- Lucieer, A., Jong, S.M.d., Turner, D., 2014a. Mapping landslide displacements using structure from motion (SfM) and image correlation of multi-temporal UAV photography. *Prog. Phys. Geogr.* 38, 97–116. <http://dx.doi.org/10.1177/0309133313515293>.
- Lucieer, A., Malenovsky, Z., Veness, T., Wallace, L., 2014b. HyperUAS-imaging spectroscopy from a multirotor unmanned aircraft system: HyperUAS-imaging spectroscopy from a multirotor unmanned. *J. Field Robot.* 31, 571–590. <http://dx.doi.org/10.1002/rob.21508>.
- Mac Arthur, A., MacLellan, C.J., Malthus, T., 2012. The fields of view and directional response functions of two field Spectroradiometers. *IEEE Trans. Geosci. Remote Sens.* 50, 3892–3907. <http://dx.doi.org/10.1109/TGRS.2012.2185055>.
- Malenovsky, Z., Turnbull, J.D., Lucieer, A., Robinson, S.A., 2015. Antarctic moss stress assessment based on chlorophyll content and leaf density retrieved from imaging spectroscopy data. *New Phytol.* 208, 608–624. <http://dx.doi.org/10.1111/nph.13524>.
- Marshall, M., Thenkabail, P., 2015. Developing in situ non-destructive estimates of crop biomass to address issues of scale in remote sensing. *Remote Sens.* 7, 808–835. <http://dx.doi.org/10.3390/rs70100808>.
- Milton, E.J., Schaepman, M.E., Anderson, K., Kneubühler, M., Fox, N., 2009. Progress in field spectroscopy. *Remote Sens. Environ.* 113, S92–S109. <http://dx.doi.org/10.1016/j.rse.2007.08.001>.
- Näsi, R., Honkavaara, E., Lyytikäinen-Saarenmaa, P., Blomqvist, M., Litkey, P., Hakala, T., Viljanen, N., Kantola, T., Tanhuanpää, T., Holopainen, M., 2015. Using UAV-based photogrammetry and hyperspectral imaging for mapping bark beetle damage at tree-level. *Remote Sens.* 7, 15467–15493. <http://dx.doi.org/10.3390/rs71115467>.
- Nicodemus, F.E., Richmond, J.C., Hsia, J.J., Ginsberg, I.W., Limperis, T., 1977. Geometrical Considerations and Nomenclature for Reflectance. National Bureau of Standards, Washington DC, pp. 67.
- Pajares, G., 2015. Overview and current status of remote sensing applications based on unmanned aerial vehicles (UAVs). *Photogramm. Eng. Remote Sens.* 81, 281–330. <http://dx.doi.org/10.14358/PERS.81.4.281>.
- Qi, J., Moran, M.S., Cabot, F., Dedieu, G., Qi, J., Moran, M.S., Cabot, F., Dedieu, G., 1995. Normalization of sun/view angle effects using spectral albedo-based vegetation indices. *Remote Sens. Environ.* 52 (3), 207–217.
- Quemada, M., Gabriel, J., Zarco-Tejada, P., 2014. Airborne hyperspectral images and ground-level optical sensors as assessment tools for maize nitrogen fertilization. *Remote Sens.* 6, 2940–2962. <http://dx.doi.org/10.3390/rs6042940>.
- Rasmussen, J., Ntakos, G., Nielsen, J., Svendsgaard, J., Poulsen, R.N., Christensen, S., 2016. Are vegetation indices derived from consumer-grade cameras mounted on UAVs sufficiently reliable for assessing experimental plots? *Eur. J. Agron.* 74, 75–92. <http://dx.doi.org/10.1016/j.eja.2015.11.026>.
- Remondino, F., El-Hakim, S., 2006. Image-based 3D modelling: a review. *Photogramm. Rec.* 21, 269–291. <http://dx.doi.org/10.1111/j.1477-9730.2006.00383.x>.
- Roosjen, P., Suomalainen, J., Bartholomeus, H., Clevers, J., 2016. Hyperspectral reflectance anisotropy measurements using a Pushbroom spectrometer on an unmanned aerial vehicle—results for barley, winter wheat, and potato. *Remote Sens.* 8, 909. <http://dx.doi.org/10.3390/rs8110909>.
- Roth, L., Streit, B., 2017. Predicting cover crop biomass by lightweight UAS-based RGB and NIR photography: an applied photogrammetric approach. *Precis. Agric.* <http://dx.doi.org/10.1007/s11119-017-9501-1>.
- Rouse Jr., J.W., Haas, R.H., Schell, J.A., Deering, D.W., 1974. Monitoring Vegetation Systems in the Great Plains with ERTS. In: *Third Earth Resources Technology Satellite-1 Symposium- Volume I: Technical Presentations*. NASA, Washington, D.C., pp. 309–317.
- Sandmeier, S.R., Itten, K., et al., 1999. A field goniometer system (FIGOS) for acquisition of hyperspectral BRDF data. *IEEE Trans. Geosci. Remote Sens.* 37, 978–986. <http://dx.doi.org/10.1109/36.752216>.
- Schaepman, M.E., 2007. Spectrodirectional remote sensing: from pixels to processes. *Int. J. Appl. Earth Obs. Geoinf.* 9, 204–223. <http://dx.doi.org/10.1016/j.jag.2006.09.003>.
- Schaepman-Strub, G., Schaepman, M.E., Painter, T.H., Dangel, S., Martonchik, J.V., 2006. Reflectance quantities in optical remote sensing—definitions and case studies. *Remote Sens. Environ.* 103, 27–42. <http://dx.doi.org/10.1016/j.rse.2006.03.002>.
- Schläpfer, D., Richter, R., Feingersh, T., 2015. Operational BRDF effects correction for wide-field-of-view optical scanners (BREFCOR). *IEEE Trans. Geosci. Remote Sens.* 53, 1855–1864. <http://dx.doi.org/10.1109/TGRS.2014.2349946>.
- Suomalainen, J., Hakala, T., Kaartinen, H., Räsänen, E., Kaasalainen, S., 2011. Demonstration of a virtual active hyperspectral LiDAR in automated point cloud classification. *ISPRS J. Photogramm. Remote Sens.* 66, 637–641. <http://dx.doi.org/10.1016/j.isprsjprs.2011.04.002>.
- Suomalainen, J., Anders, N., Iqbal, S., Roerink, G., Franke, J., Wenting, P., Hänniger, D., Bartholomeus, H., Becker, R., Kooistra, L., 2014. A lightweight hyperspectral mapping system and photogrammetric processing chain for unmanned aerial vehicles. *Remote Sens.* 6, 11013–11030. <http://dx.doi.org/10.3390/rs6111013>.
- Szeliski, R., 2011. *Computer Vision, Texts in Computer Science*. Springer London, London.
- Tilly, N., Aasen, H., Bareth, G., 2015. Fusion of plant height and vegetation indices for the estimation of barley biomass. *Remote Sens.* 7, 11449–11480. <http://dx.doi.org/10.3390/rs70911449>.
- Verrelst, J., Schaepman, M.E., Koetz, B., Kneubühler, M., 2008. Angular sensitivity analysis of vegetation indices derived from CHRIS/PROBA data. *Remote Sens. Environ.* 112, 2341–2353. <http://dx.doi.org/10.1016/j.rse.2007.11.001>.
- Weyeremann, J., Damm, A., Kneubühler, M., Schaepman, M.E., 2014. Correction of reflectance anisotropy effects of vegetation on airborne spectroscopy data and derived

- products. *IEEE Trans. Geosci. Remote Sens.* 52, 616–627. <http://dx.doi.org/10.1109/TGRS.2013.2242898>.
- Whitehead, K., Hugenholtz, C.H., 2015. Applying ASPRS accuracy standards to surveys from small unmanned aircraft systems (UAS). *Photogramm. Eng. Remote. Sens.* 81, 787–793. <http://dx.doi.org/10.14358/PERS.81.10.787>.
- Yu, K., Lenz-Wiedemann, V., Chen, X., Bareth, G., 2014. Estimating leaf chlorophyll of barley at different growth stages using spectral indices to reduce soil background and canopy structure effects. *ISPRS J. Photogramm. Remote Sens.* 97, 58–77. <http://dx.doi.org/10.1016/j.isprsjprs.2014.08.005>.
- Zarco-Tejada, P.J., González-Dugo, V., Berni, J.A.J., 2012. Fluorescence, temperature and narrow-band indices acquired from a UAV platform for water stress detection using a micro-hyperspectral imager and a thermal camera. *Remote Sens. Environ.* 117, 322–337. <http://dx.doi.org/10.1016/j.rse.2011.10.007>.
- Zhao, F., Li, Y., Dai, X., Verhoef, W., Guo, Y., Shang, H., Gu, X., Huang, Y., Yu, T., Huang, J., 2015. Simulated impact of sensor field of view and distance on field measurements of bidirectional reflectance factors for row crops. *Remote Sens. Environ.* 156, 129–142. <http://dx.doi.org/10.1016/j.rse.2014.09.011>.